

Estimating snow accumulation and ablation with L-band InSAR

Jack Tarricone^{1,2}, Ryan W. Webb³, Hans-Peter Marshall⁴, Anne W. Nolin^{2,1}, and Franz J. Meyer⁵

¹Graduate Program of Hydrologic Sciences, University of Nevada, Reno, Reno, NV, USA

²Department of Geography, University of Nevada, Reno, Reno, NV, USA

³Department of Civil & Environmental Engineering & Construction Management, University of Wyoming, Laramie, WY, USA

⁴Department of Geosciences, Boise State University, Boise, ID, USA

⁵Geophysical Institute, University of Alaska Fairbanks, Fairbanks, AK, USA

Correspondence: Jack Tarricone (jtarricone@nevada.unr.edu)

Abstract. Snow is a critical water resource for the western US and many regions across the globe. However, our ability to accurately measure and monitor changes in snow mass from satellite remote sensing, specifically its water equivalent, remains a challenge ~~in mountain regions~~. To confront these challenges, NASA initiated the SnowEx program, a multi-year effort to address knowledge gaps in snow remote sensing. During SnowEx 2020, the ~~UAVSAR~~ Uninhabited Aerial Vehicle SAR (UAVSAR) team acquired an L-band Interferometric Synthetic Aperture Radar (InSAR) data time series to evaluate the capabilities and limitations of repeat-pass L-band InSAR ~~data~~ for tracking changes in snow water equivalent (SWE). The goal was to develop a more comprehensive understanding of where and when L-band InSAR can provide ~~snow mass~~ SWE change estimates, allowing the snow community to leverage the upcoming NASA-ISRO SAR (NISAR) mission. Our study analyzed three InSAR image pairs from the Jemez ~~River~~ Mountains Basin, NM, between ~~12-26-12-26~~ February 2020. We developed ~~an end-to-end UAVSAR InSAR processing workflow for snow applications. This open-source approach employs a novel data fusion method that merges optical~~ a snow-focused multisensor method that uses UAVSAR InSAR data synergistically with optical fractional snow covered area (SCA) ~~information with InSAR data~~ fSCA information. Combining these two remote sensing datasets allows for atmospheric correction and delineation of snow covered pixels within the radar swath. For all InSAR pairs, we converted phase change values to SWE change estimates between the three ~~data~~ acquisition dates. We then ~~evaluated InSAR-derived retrievals using a combination of optical snow cover data~~ fSCA, snow pits, meteorological station data, in situ snow depth sensors, and ground-penetrating radar (GPR). The results of this study show that repeat-pass L-band InSAR is effective for estimating both snow accumulation and ablation with the proper measurement timing, reference phase, and snowpack conditions.

1 Introduction

20 1.1 Significance and Motivation

In the western US (WUS), seasonal mountain snowmelt produces approximately 70 % of the annual discharge (Li et al., 2017a), and is the primary water source for about 60 million people (Stewart et al., 2004). To adequately manage this resource,

an accurate accounting of the spatiotemporal variations in snow water equivalent (SWE) is needed (Bales et al., 2006). Climate change is affecting the stationarity of the WUS hydrologic cycle (Milly et al., 2008), causing an overall decline in mountain snowpack (Mote et al., 2018), and emphasizing the importance of properly monitoring snow into the future (Siirila-Woodburn et al., 2021).

Water managers could benefit from regular repeat coverage of spatially distributed, ~~low-latency-low-latency~~ SWE data at spatial resolutions that are appropriate for mountain water forecasting. While remote sensing has made significant advances in measuring snow properties, there is still no remote sensing technique that can continually measure SWE from space for mountain hydrologic applications (Lettenmaier et al., 2015). Here, we explore L-band InSAR for monitoring changes in SWE.

1.2 Background and Previous Work

The most effective and widely used SWE estimation technique combines suborbital lidar (~~Deems et al., 2006; ?~~) (~~Deems et al., 2006; Trujillo et al., 2018~~) with hyperspectral imaging (Nolin et al., 1993) to produce both snow depth and fractional snow covered area (fSCA) at the watershed scale. ~~To convert~~ Converting these measurements into SWE requires spatially distributed snowpack energy balance modeling (Painter et al., 2016). Like all optical techniques, lidar and hyperspectral imaging are limited by cloud cover, which can be frequent in mountain environments, and global spaceborne monitoring with lidar is not currently practical.

Since the ~~1970's~~ 1970s, spaceborne passive microwave radiometers have used brightness temperature to estimate SWE at hemispherical scales (Rango et al., 1979). More recent studies utilized the Advanced Microwave Scanning Radiometer-EOS (ASMR-E) and the Scanning Multichannel Microwave Radiometer (SMMR) to continue the development of this SWE estimation technique (Derksen et al., 2002; Vuyovich et al., 2014). These instruments produce data on the spatial scale of tens of kilometers, limiting their ability to capture the topographic and snowpack heterogeneity of mountain environments. Passive microwave retrievals are also limited to dry snowpacks ~~less than approximately 1~~ $\lesssim 1$ m of snow depth due to signal saturation (Foster et al., 2005).

While passive microwave remote sensing is not well suited for mountain environments, active microwave (radar) has shown promise for snowpack monitoring. Time-of-flight approaches have been used for decades from ground-based (Gubler and Hiller, 1984; Marshall and Koh, 2008) and airborne (McGrath et al., 2018; Lewis et al., 2017) platforms. Synthetic aperture radar (SAR) is an active microwave remote sensing technique that addresses the two main deficiencies in both optical and passive microwave; it can penetrate through clouds and has a spatial resolution on the scale of tens of meters instead of kilometers.

Spaceborne applications of SAR for estimating snow properties have mostly focused on backscatter approaches, where shorter wavelengths (Ku- and X-band) have been used to estimate SWE (Rott et al., 2010; Yueh et al., 2009; King et al., 2018; Zhu et al., 2021). However, this method requires a complex dense media radiative transfer model (DMRT) with input parameters that not only include snow density (ρ_s) and snowpack liquid water content (LWC), but also parameters such as snow stratigraphy, snow grain size, and ground surface conditions. ~~The snow~~ Snow microstructure parameters are challenging to precisely estimate over large spatial scales (Rutter et al., 2019).

SAR is proven for measuring snow wetness (Nagler and Rott, 2000; Nagler et al., 2016; Lund et al., 2020) as wet snow attenuates the radar signal, causing a decrease in backscatter intensity when compared to dry snow conditions. New backscatter methods are being developed to measure snow depth at C-band (Lievens et al., 2019, 2022). This technique shows promise, especially in deeper snowpacks (>1 m), but the underlying physics governing the retrievals are not yet well characterized.

60 Recently, the use of Interferometric Synthetic Aperture Radar (InSAR) to estimate SWE has become an area of interest because of the higher temporal (12 days) frequency and L-band (~24 cm) wavelength of the future NASA-ISRO SAR (NISAR) mission (Rosen et al., 2017). InSAR uses the differences in radar phase between subsequent overpasses to estimate surface displacement. The InSAR SWE theory, initially proposed by [Gunteriusen et al. \(2001\)](#), relates changes in the interferometric phase of a radar signal to ~~changes in mass~~ [SWE changes](#) of dry snow on the ground between acquisitions.

65 A series of studies have shown [the](#) further utility of these InSAR methods for snow, such as Rott et al. (2003) in Austria, and Deeb et al. (2011) on Alaska's north slope using European Remote-Sensing Satellite (ERS-1) C-band radar. Leinss et al. (2015) conducted an intensive season-long ground-based dual-frequency (Ku- and X-band) interferometric experiment in Finland with measurements every four hours, where they found the method was successful for continually measuring SWE in dry taiga snow, but that liquid water and vegetation quickly cause coherence loss at these higher frequencies.

70 More recent studies have also used C-band radar from various space-borne platforms. The Sentinel-1 A/B radar was utilized in Finland, leveraging the more consistent overpass repeat cycle (Conde et al., 2019). Li et al. (2017b) analyzed two InSAR pairs [from the](#) Envisat ASAR instrument in [the](#) Tianshan Mountains of northwestern China, where they found promising results but were limited by large interferometric temporal baselines and the lack [of](#) in situ validation data. Eppler et al. (2022) used a ~~nine-year~~ [nine-year](#) RADARSAT-2 time series in Canada to develop "SlopeVar", a method for estimating SWE change without phase unwrapping by spatially correlating phase sensitivity to local topography. Nagler et al. (2022) conducted an airborne L- and C-band experiment in the Austrian Alps in preparation for Radar Observation System for Europe in L-band (ROSE-L). While their results are preliminary, they show good performance for tracking snowfall events at L-band because of ~~its~~ [its](#) lack of impairment from 2π phase wrapping ambiguities.

80 These orbital InSAR studies showed promise for estimating SWE but lacked sufficient temporal length and variety of vegetation, topography, and snowpack characteristics. Moreover, they also lacked adequate validation data and [a](#) small spatial scale to thoroughly understand the technique's limitations and synergies with other types of snow measurements.

1.3 Research Objectives

To address these InSAR-derived SWE limitations, the 2020 NASA SnowEx campaign ~~(?)~~ [\(Marshall et al., 2019\)](#) conducted an Uninhabited Aerial Vehicle Synthetic Aperture Radar (UAVSAR) L-band InSAR time series flight campaign at 13 research sites across the WUS. The goal of the 2020 SnowEx experiment was to test L-band InSAR's ability to measure SWE changes in a wide range of geographic locations, snow conditions, and land cover types with corresponding in situ ground-based observations. InSAR-derived snow depth changes measured over a ~~two-week~~ [two-week](#) interval on the open western end of Grand Mesa, CO in February 2020 showed high correlation ($r^2 =$ ~~0.76~~[0.76](#)) with snow depth differences measured by coincident

repeat lidar from the same time period. RMSE differences between the two 5 m resolution depth change maps ~~was were~~ within
90 typical lidar error (~~<5 cm>~~ 5 cm) for depth and 0.9 cm of SWE (Marshall et al., 2021).

The overall goal of this study is to assess the performance of L-band InSAR for monitoring SWE changes in an environment where there is both snow accumulation and ablation ~~Currently (melt, evaporation, or sublimation)~~. Currently,
this UAVSAR-based approach has only been applied to cold dry snow conditions ~~with accumulation and on Grand Mesa~~
(Marshall et al., 2021), where the snow depth variations were mainly driven by wind redistribution, but not melt or evaporation.
95 Towards this end, the specific objectives of the work presented here are to (1) analyze InSAR SWE retrievals over a complex mountain region ~~and~~ (2) validate the retrievals using satellite and in situ data.

2 Methods

To achieve our objectives, we analyzed three interferometric image pairs that were acquired over the Jemez Mountains, New Mexico (Figure 2a). First, we developed a ~~novel open-source processing work flow workflow~~ (Tarricone, 2023) that (a) corrects
100 the observed interferometric phase for atmospheric delay and (b) corrects incidence angle error effects by using improved incidence angle estimates derived from airborne lidar. We then computed spatial changes in SWE over the study area (Figure 2e), and evaluated our SWE retrievals using ~~optical fSCA, ultrasonic snow depth sensors, GPR, and in situ snow depth measurements~~ ground-penetrating radar (GPR), and snow pits.

Section 2 (Methods) is split into the following subsections: 2.1 overviews InSAR for estimating SWE changes, 2.2 describes the study area, 2.3 reviews the remote sensing and in situ data, 2.4 is a description of the atmospheric correct steps, 2.5 explains the creation of new incidence angle data, and 2.7 outlines the SWE change calculation.
105

2.1 InSAR for detecting SWE changes

InSAR is an active remote sensing technique that uses the differences in phase to map surface topography (single-pass) (Zebker and Goldstein, 1986) or ~~measure changes to the Earth's surface various types of surface deformation~~ (repeat-pass) (Goldstein
110 and Zebker, 1987). Using the precise location of the orbit or flight pattern, the phase difference between the two (repeat-pass) acquisitions can be used to calculate deformation on the centimeter scale. Traditionally repeat-pass InSAR (Rosen et al., 2000), where the sensor scans the same area at two different times, has been used to ~~map tectonic and geomorphic activity on the Earth's surface~~ monitor tectonic motion (Funning et al., 2005), geomorphic processes (Colesanti et al., 2003), ice sheet velocity (Mouginot, 2012), and volcanic activity (Mouginot, 2012; Rosen et al., 2000) (Poland and Zebker, 2022).

115 For snow applications, ~~?~~ Guneriussen et al. (2001) theorized a relationship between InSAR phase change and ~~variation in dry snow water equivalent (SWE) change in dry SWE~~ between acquisitions. Dry snow has ~~a low attenuation rate~~ low attenuation of the radar signal, and at frequencies below 10 GHz (Marshall et al., 2005; Ulaby et al., 1984), the majority of the backscatter stems from the snow ground interface. Dry snow and the atmosphere have different dielectric properties, causing a refraction or directional change of the radar propagation path ~~and~~ a decrease in speed when the signal propagates through the snow layer

120 (Figure 1). The refraction and wave speed are controlled by the refractive index of snow, which is governed by ρ_s . We leverage these previous studies to develop a current workflow applied to UAVSAR data acquisitions.

To isolate the SWE change impacts on the phase, other factors impacting phase must be identified and compensated for. Outlined in Deeb et al. (2011) [and updated for suborbital acquisition considerations](#), total interferometric phase includes the following contributions:

$$125 \quad \phi_{total} = \phi_{flat} + \phi_{topo} + \phi_{atm} + \phi_{snow} + \phi_{noiserandom} + \phi_{systematic} \quad (1)$$

where ϕ_{flat} and ϕ_{topo} are phase impacts from [the](#) flat Earth and local topography, which are both ~~already~~ accounted for in the UAVSAR InSAR processing chain using the Shuttle Radar Topography Mission (SRTM) DEM as input. ~~For UAVSAR,~~ $\phi_{noiserandom}$ is the random error, where the majority comes from temporal decorrelation (Zebker et al., 1997). $\phi_{systematic}$ represents the systematic error within the UAVSAR instrument. This error is mainly associated with uncertainty ~~with in~~ the plane's ~~GPS and slight variations in path between the two acquisitions. These errors are also~~ position and deviations in the flight track between acquisitions. Variations in the plane's position are accounted for within the UAVSAR processing workflow. ~~Hence, for UAVSAR dataas best as possible, but not all aircraft motion can be completely captured, which can leave residual phase change.~~

~~Assuming all previously mentioned errors are accounted for,~~ extracting ϕ_{snow} from the observed phase (ϕ_{total}) in UAVSAR data mostly requires an accurate compensation of ϕ_{atm} , which is the phase ~~influence from~~ contribution from change in path delay through the atmosphere. Refer to ~~Section-Subsection~~ 2.4 for a detailed explanation of how ϕ_{atm} is addressed in our approach.

Once ϕ_{snow} is isolated, the measured phase shifts are used to estimate SWE using the following equation proposed by ~~?~~ [Gunteriusen et al. \(2001\)](#), which accounts for both the path length change caused by refraction ~~;~~ and the change in wave speed in snow:

$$140 \quad \Delta SWE = -\frac{\Delta \phi_{snow} \lambda}{4\pi} \cdot \rho_s \cdot \frac{1}{\cos \theta - \sqrt{\epsilon_s - \sin^2 \theta}} \quad (2)$$

where ΔSWE is [the](#) change in SWE between acquisitions, λ is the radar wavelength (23.84 cm for UAVSAR), θ is the radar incidence angle, and ϵ_s is the real part of the dielectric permittivity of snow. For dry snow, there is a direct relationship between ϵ_s and ρ_s , ~~whereas for wet snow, the relationship becomes more complex, with even small amounts of liquid water vastly increasing ϵ_s values.~~ Recent studies from [Eppler et al. \(2022\)](#) and [Leinss et al. \(2015\)](#) found that error in density estimates only biases total SWE change by $< \sim 5\%$ for dry snow in a wide range of θ ($< 50^\circ$) and ρ_s ($< 500 \text{ kg m}^{-3}$). [Leinss et al. \(2015\)](#) also showed a nearly linear relationship between ΔSWE and interferometric phase for dry snow, which simplifies the SWE estimation. That said, we used Equation 2 because our study considers melting snow and ϵ_s is a direct input.

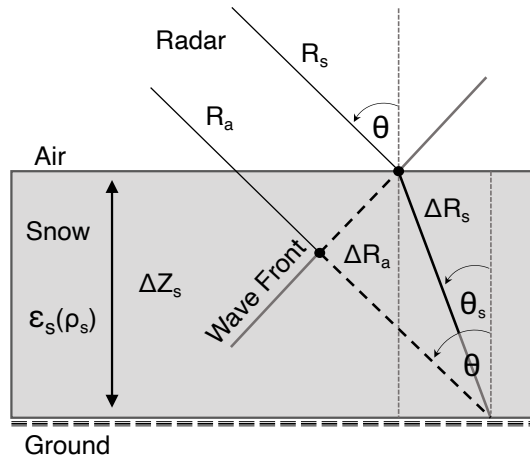


Figure 1. (Left) Graphic Diagram adapted from Leinss et al. (2015) showing the factors affecting radar ϕ_{total} for airborne and orbital SAR geometric principle of the InSAR SWE retrieval. R_a represents propagation through atmosphere (Right) Diagram of how radar wave propagates with no snow (ΔR_a) and R_s (with snow ($\Delta R_a + \Delta R_s$)) at a certain radar incidence angle (θ) to the wave front. The amount of refraction (θ_s) and change in wave speed are controlled by the snow dielectric permittivity (ϵ_s), which is a function of snow density (ρ_s). The variation in path length with and without snow is equal to $\Delta R_s - \Delta R_a$. This path length difference causes a phase delay which is used to estimate SWE changes.

2.2 Description of the Study Area

150 Located in northern New Mexico, U.S.A., the Jemez Mountains and Jemez River Basin are on the southern extent of the Rocky Mountains (Figure 2a2b). The extent of the UAVSAR swath encompasses portions of Valles Caldera National Preserve (VCNP) (35°53'N, 106°32'W) (Figure 2b2a). This area is mainly a mountain conifer forest environment consisting of Douglas fir, white fur, and blue spruce. VCNP is surrounded by lower elevation semi-arid desert. Within the swath also lies the Valles Caldera, a 25-km-25 km wide volcanic structure dating back about 1.2 million years. Within Valles Caldera, VCNP is Valle Grande (VG) (Figure 2e) is 2f), an extensive open grassland where field measurements took place for this study. Many resurgent lava domes form peaks over the grassy valleys, the highest of which is Redondo Peak (3430 m a.s.l.). About 50 % of the total annual precipitation falls in the summer months as rain from convective monsoonal storms, and the rest falls in the winter as snow. The water in this area drains into the East Fork of the Jemez River and eventually to the Rio Grande. The nearby Quemazon Natural Resource Conservation Services (NRCS) Snow Telemetry (SNOTEL) site (35°55'N, 106°24'W, 2898 m a.s.l.) has a 1980-2022-1980-2022 average peak SWE of 22.4 cm.

(a) Map showing the area of the UAVSAR acquisition (black outline) in the Jemez Mountains, NM. (b) DEM of the UAVSAR acquisition provided by NASA, with a black rectangle outlining VG and the surrounding hill slopes. (c) Lidar DEM of VG with the two snow pit locations shown by yellow circles, HQ meteorologic station by a blue triangle, six CZO snow depth sensors by black diamonds, and the GPR transect shown as a black line. (d) A close up of the GPR transect with the HQ

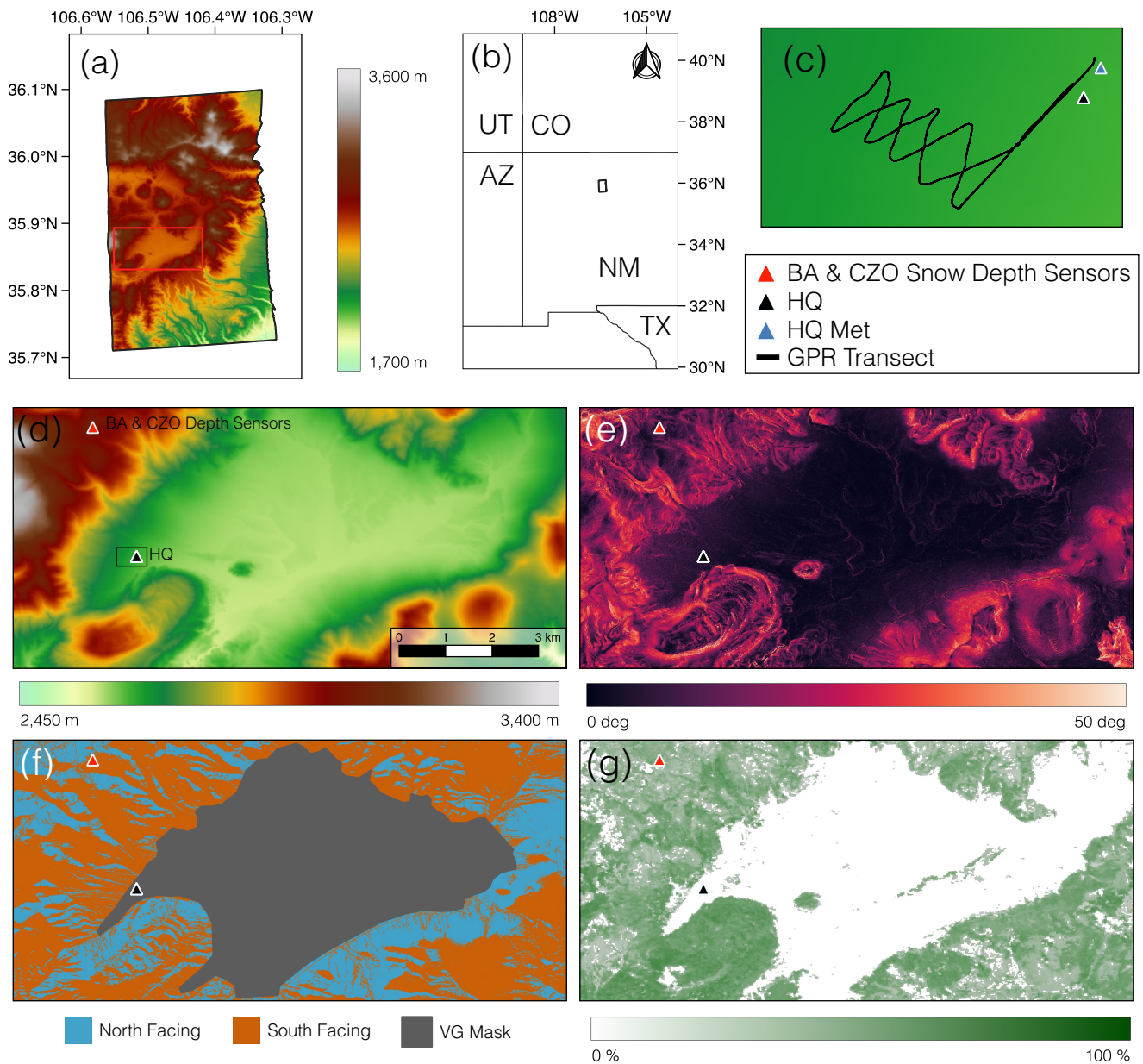


Figure 2. (a) DEM of the UAVSAR acquisition area provided by NASA, with a red rectangle outlining the study area. (b) Map showing the area of the UAVSAR acquisition (black outline) in the Jemez Mountains, NM. (c) A close-up of the GPR transect outlined by the black rectangle in (d), with the HQ Met (blue triangle) and HQ snow pit (black triangle) displayed. Due to their close proximity, a single red triangle represents the BA pit and CZO snow depth sensors. Within the study area extent: (d) lidar DEM, (e) lidar-derived slope, (f) lidar aspect binned to north (270-90°) (blue) and south (90-270°) (orange) facing slopes, with the gray area representing the flat VG meadow where aspect values are not valid, and (g) NLCD canopy cover percentage.

165 ~~Met snow pit and meteorologic station displayed.~~ We focus our analysis on an 82.5 km² section of the UAVSAR swath that encompasses VG and the surrounding forested hillslopes. The study area is defined by the red rectangle in Figure 2a, with inset maps showing elevation (Figure 2d), slope (Figure 2e), binned north and south aspects with VG delineated (Figure 2f), and 2016 NLCD canopy cover percentage (Figure 2g).

2.3 Data Description

170 2.3.1 Remote Sensing data UAVSAR

UAVSAR is a fully polarimetric L-band radar deployed on a NASA Gulf Stream III aircraft, traditionally flown at ~13,700 m with a ~~16–22~~ km nominal swath width (Hensley et al., 2008; Rosen et al., 2006). Detailed technical specifications of the radar are provided ~~in at the top of~~ Table 1.

~~UAVSAR data was UAVSAR data were~~ accessed using the Python package `uavsar_pytools` (Keskinen and Tarricone, 2022).
175 It ~~utilizes uses the~~ `asf_search` API (https://github.com/asfadmin/Discovery-asf_search) for easier downloading, formatting, and analysis of UAVSAR data. The flights used in this study occurred ~~in on~~ the mornings of 12, 19, and 26 February 2020 (Table 2). ~~The 12–19 and 19–26 February InSAR pairs were processed by the 2020. The~~ UAVSAR team at the NASA Jet Propulsion Laboratory (JPL) ~~, where they processed two 7-day (12–19 and 19–26 February) and one 14-day (12–26 February) ground projected (GRD) InSAR pairs. They~~ were unwrapped using the Integrated Correlation and Unwrapping (ICU) algorithm
180 (Goldstein et al., 1988). ~~The 12–26 February pair was processed locally from a Single Look Complex (SLC) stack using the Interferometric synthetic aperture radar Scientific Computing Environment (ISCE2) and unwrapped with the Statistical Cost, Network-Flow Algorithm for Phase Unwrapping (SNAPHU) algorithm (Chen and Zebker, 2001).~~

~~Landsat 8 fSCA (U.S. Geological Survey and Center, 2018) data was acquired for 18 February and 5 March 2020 (Figure Processing parameters are outlined at the bottom of Table 1, and information about the specific products used is provided~~
185 ~~in the Supplement. For the three flights used in this study, the flight track baseline was maintained within $< \pm 3$). This data is generated using a spectral unmixing analysis based Snow Covered Area and Grain size (SCAG) algorithm developed for MODIS (Painter et al., 2009). The data processing workflow includes water masking, cloud masking, and canopy cover corrections (Selkowitz et al., 2017).~~

~~Landsat derived fSCA in the UAVSAR swath extent from (a) 18 February 2020 (b) 5 March 2020. Snow melt between~~
190 ~~these two days caused both a reduction in scene wide SCA and fSCA within the VG meadow. m, which is within the $< \pm 5$ m requirement (Hensley et al., 2008).~~

~~Three interferometric products: coherence, unwrapped phase, and the interferogram are produced for each InSAR pair. Coherence measures the consistency of the scattering characteristics within a pixel between InSAR acquisitions. Unwrapped phase is the estimated absolute phase change in a pixel, generated from the initially ambiguous interferogram, which is defined~~
195 ~~modulo 2π .~~

~~When there is a significant change in the landscape scattering properties between InSAR acquisitions, phase noise and fringe discontinuities increase, coherence decreases, and the unwrapping algorithm performs less reliably (Balzter, 2001).~~

Table 1. Technical Specifications of the UAVSAR L-band radar ([top](#)). [InSAR processing and data parameters \(bottom\)](#).

Parameter	Value
Wavelength	23.84 em cm
Frequency	1.26 GHz GHz
Polarization	Quad Pol
Bandwidth	800 MHz 80 MHz
Pulse Length	40 μ s
Radar Look Direction	Left
Range Swath Width	16 km 22 km
Ground Range Pixel Spacing 6 m Azimuth Spacing 7.2 m Slant Range Spacing 4.99 m Average Near Range Look Angle	28.01°
Average Far Range Look Angle	68.9°
Ground Range Pixel Spacing	6 m
Number of Looks in Range	3
Number of Looks in Azimuth	12
Phase Unwrapping Method	ICU
Phase Unwrapping Filtering Method	Low Pass
Phase Unwrapping Filter Window Size	3 × 3 pixels

Table 2. [UAVSAR unwrapped phase \(UNW\) and coherence statistics for the full scene \(FS\) and study area \(SA\)](#). UNW Loss (%) is the percentage of pixels lost in the unwrapping process.

Pair	Polarization	FS Mean Coherence	SA Mean Coherence	FS UNW Loss (%)	SA UNW Loss (%)
12–19 Feb.	HH	0.53	0.50	9.4	7.7
12–19 Feb.	VV	0.54	0.50	8.9	12.8
19–26 Feb.	HH	0.55	0.52	5.0	4.1
19–26 Feb.	VV	0.57	0.54	4.3	3.7
12–26 Feb.	HH	0.50	0.48	8.3	6.6
12–26 Feb.	VV	0.53	0.51	6.7	5.5

We analyzed the coherence and unwrapped phase products for the HH and VV polarizations to assess their quality before implementing the SWE change equation. We found co-polarizations performed similarly (Table 2), and choose to utilize HH for our study.

The right side of Figure 3 shows the coherence values in the study area for (a) 12–19 February, (b) 19–26 February, and (c) 12–26 February. In the coherence maps, there are clear patterns with respect to topography and probable variations in snowpack

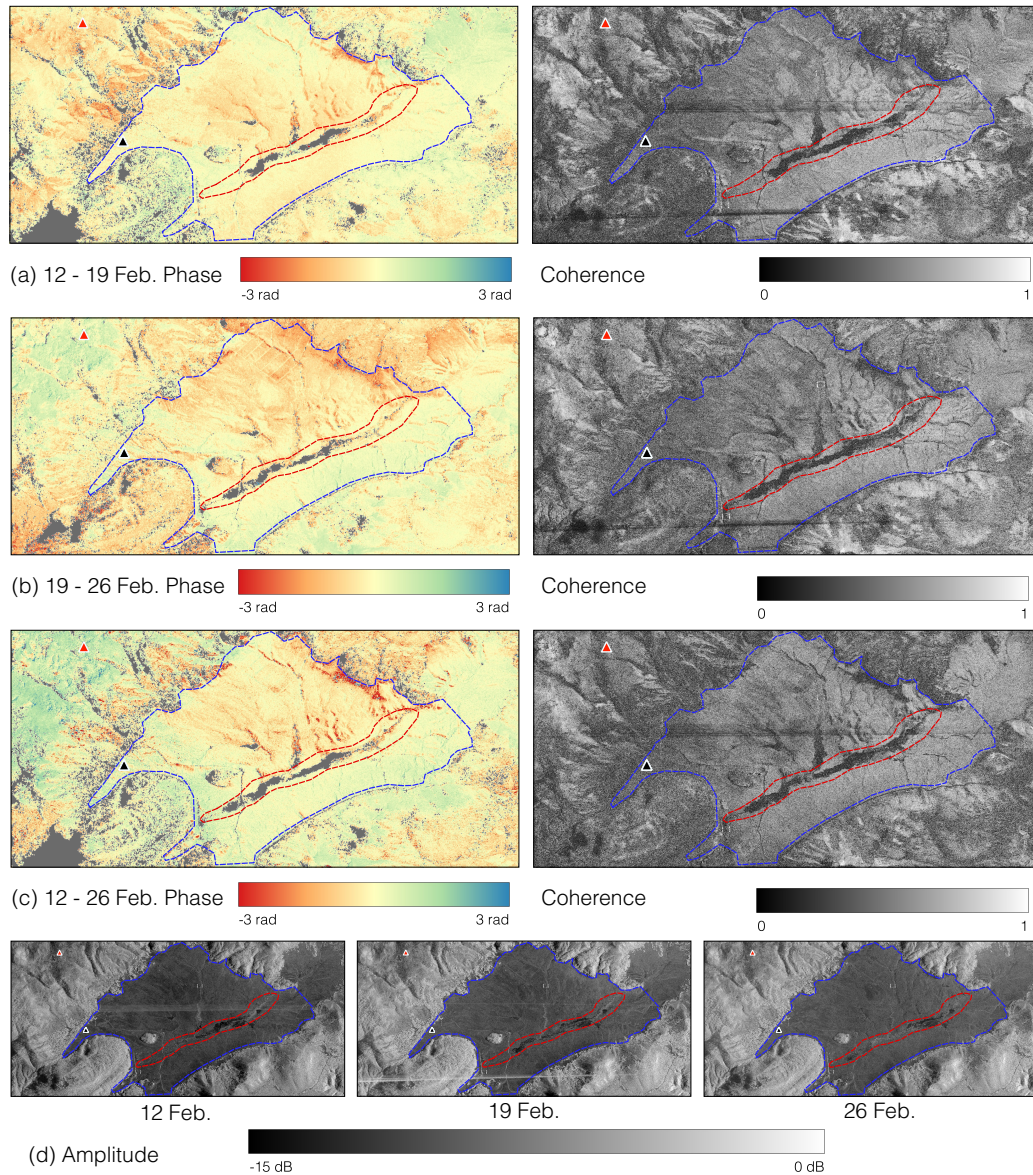


Figure 3. The unwrapped phase and coherence data for the (a) 12–19 February, (b) 19–26 February, and (c) 12–26 February InSAR pairs. The amplitude data (d) for the three UAVSAR flights. Both (a) and (c) were atmospherically corrected. The gray area in the phase data are pixels lost in the unwrapping processes. VG and Jemez River main channel are outlined by blue and red dotted lines, respectively. Triangles show the BA (red) and HQ (black) pits.

LWC. The area of lowest coherence surrounds the main channel of the Jemez River (red dotted line) that flows through the south-central portion of VG. As seen in Figure 3d there is a variable area of low backscatter in all three amplitude images. This

205 backscatter decrease is likely caused by snowpack LWC or subnivean surface water attenuating the radar signal. The spatial variability in backscatter values in this riparian area between acquisitions causes low coherence and the loss of pixels in the unwrapping processes for all three pairs. There are also horizontal streaks of low coherence and high backscatter within the images. These are likely a result of radio frequency interference (RFI) during the acquisitions. These lines do not propagate into the unwrapped phase data and therefore are not of concern.

210 The left side of Figure 3a–c displays the unwrapped phase values for the three InSAR pairs. The 12–19 February and 12–26 February pairs show the atmospherically corrected data, with this methodology discussed in Section 2.4. In the open VG meadow (blue dotted line), the unwrapping algorithm performs well, and most pixels are preserved except in the riparian area for the reasons described previously. The other source of low coherence and corresponding unwrapping pixel loss occurs on the forested hill slopes (outside of the blue dotted line) surrounding the VG meadow. Overall, the unwrapped data provides a
215 high-quality input into the SWE change inversion equation.

2.3.2 Landsat fSCA

No current technique can confidently discriminate dry snow cover using solely L-band radar (Tsai et al., 2019). Our study aims to assess the ability of L-band InSAR to estimate spatiotemporal SWE changes. Therefore, our analysis requires properly identifying snow covered pixels within the UAVSAR swath, ensuring the radar signal interacts with mostly snow cover and not
220 bare ground. To do this, we utilized Landsat 8 fSCA (U.S. Geological Survey and Center, 2018) data from 18 February and 5 March 2020 (Figure 4). These data are generated using a spectral unmixing analysis based on the Snow Covered Area and Grain size (SCAG) algorithm developed for MODIS (Painter et al., 2009). The data processing workflow includes water masking, cloud masking, and canopy cover corrections (Selkowitz et al., 2017; Stillinger et al., 2023). Within the full UAVSAR swath, 29.7 % of pixels were entirely snow free on 18 February (Figure 4a), increasing to 38.1 % on 5 March (Figure 4b). For just the
225 study area, 4.1 % of pixels were snow free on 18 February (Figure 4d), with an increase to 9.1 % by 5 March (Figure 4e).

2.3.3 Snow Pit and Meteorologic Station Data

Snowpack information was collected at two pit locations during each of the three UAVSAR overflights (Marshall et al., 2022) –. These data are stored in the SnowEx database (Johnson and Sandusky, 2023). The Headquarters Meteorologic station (HQ Met) pit was located at 35°51'30"N, 106°31'17"W, at an elevation of 2650 m. The Burned Area (BA) pit was located near
230 Redondo ~~peak-Peak~~ at 35°53'18"N, 106°31'57"W, at an elevation of ~~3045 m (Figure 2e)~~3030 m.

Measurements of snow depth, ~~stratigraphy,~~ snow layer stratigraphy (grain size, grain shape, hand hardness, and manual wetness), ρ_s , ϵ_s , ~~temperature, and grain size and temperature~~ were recorded for each pit. ρ_s , ϵ_s , and temperature were measured in 10 cm increments starting at the top of the pit. Stratigraphic layer size is variable and defined by the observer. In situ ρ_s measurements have been shown to have an uncertainty of ~10 % (Conger and McClung, 2009; Proksch et al., 2016). ϵ_s was
235 measured using an A2 Photonics WISE instrument (A2P, 2021) –, which Webb et al. (2021b) showed to have a mean absolute error (MAE) of 0.106 when compared to other in situ observations.

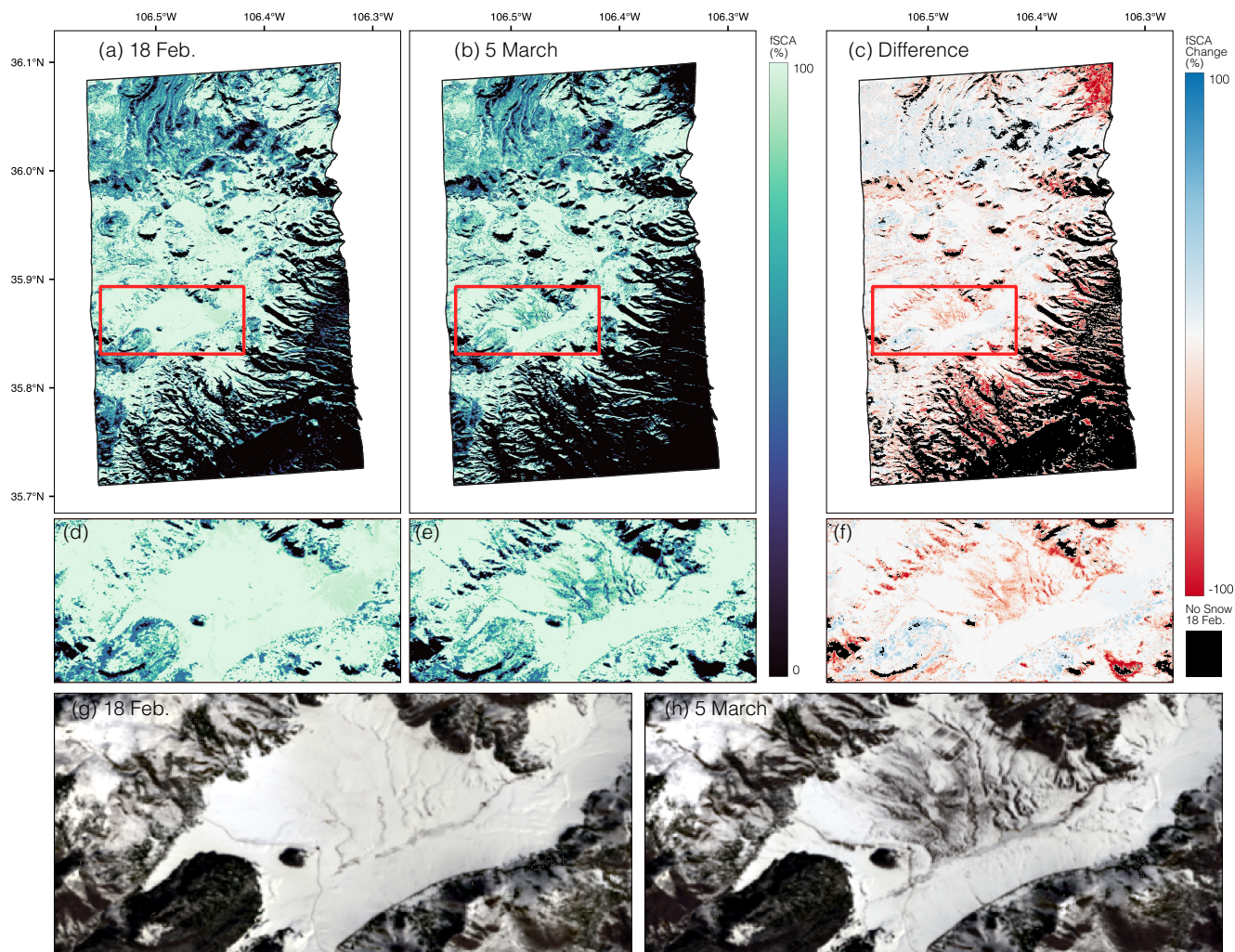


Figure 4. Landsat fSCA clipped to the UAVSAR swath extent (black outline) for (a) 18 February 2020 and (b) 5 March 2020. (c) The pixel-wise percent fSCA change between the two dates, with the black area representing 0 % fSCA from 18 February 2020. The study area fSCA (red box) for (d) 18 February 2020, (e) 5 March 2020, (f) and the difference between the two dates. Landsat true color image in the study area for (g) 18 February 2020 and (h) 5 March 2020.

Summary statistics from each pit are located in Table [2-3](#). Interval boards, which are small plastic manual precipitation gauges placed on the snow surface used to track new snow accumulation, were located in close proximity to **each of the two snow pits** both snow pits. The HQ pit data noted minor melting for both the 20 and 26 February, and it is important to clarify that the snow pits were collected ~1–3 hours after the radar data acquisition.

The Western Climate Research Center (WRCC) deployed two meteorologic stations that measured snow depth ([Figure 5a](#)), air temperature ([Figure 5b](#)), wind speed, **wind direction**, ([Figure 5c](#)), and incoming solar radiation ([Figure 5d](#)). The first station

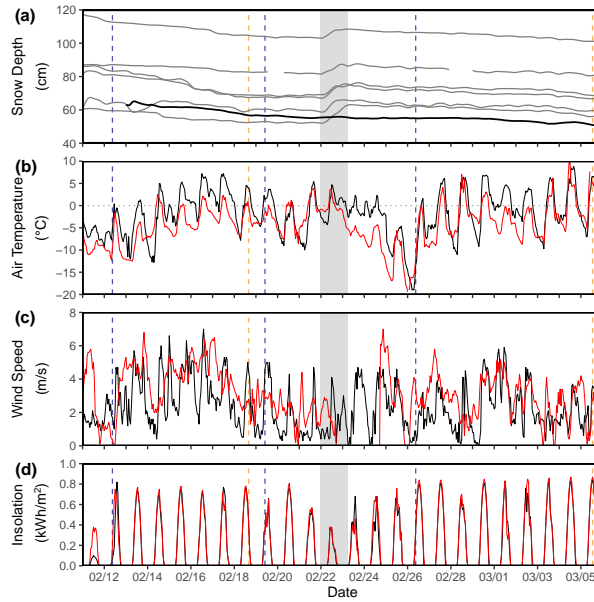


Figure 5. (a) A snow depth time series of the six CZO snow depth sensors (gray lines) (~3030 m) and HQ Met (black) (2650 m). The gray-shaded area represents a small storm registered by the sensors on Redondo Peak. HQ Met and RP Met (red) (3231 m) time series of (b) average hourly temperature, (c) average hourly wind speed, (d) and average hourly incoming solar radiation (insolation) from 11 February to 6 March. The vertical blue dotted lines represent the three UAVSAR flights (12, 19, 26 February), and the vertical orange dotted lines represent the Landsat fSCA acquisitions (19 February and 5 March).

is the aforementioned HQ station Met, and the second is located on Redondo Peak near the BA pit ((RP Met) (35°53'02"N, 106°33'13")). Six ultrasonic snow depth sensors (~3030 m) originally installed by Molotch et al. (2009) and utilized-used in subsequent studies by (Musselman et al., 2008; Harpold et al., 2015), were used to measure variations in snow depth near the BA pit (Figure 2c). Ultrasonic snow depth sensors have a known uncertainty of ± 1 cm (Ryan et al., 2008).

Figure 5 is a time series of in situ meteorologic data from HQ Met and RP Met. Figure 5a shows snow depths from seven ultrasonic sensors from 11 February to 6 March. The gray-shaded area on the plot shows a small snowfall event starting the night of 22 February and ending 23 February. In situ snow depths were converted to SWE by multiplying by the bulk ρ_s (from snow pit observations) for the 12–19 and 12–26 February pairs. We used a ρ_s of 240 kg m^{-3} for new snow measured from the BA pit interval board for the 19–26 February pair.

2.3.4 GPR Survey

We used Ground Penetrating Radar (GPR) to obtain distributed SWE estimates GPR to estimate SWE along a transect for ground-validation purposes (Marshall et al., 2005; Webb, 2020). ground-based validation near the HQ site (Marshall et al., 2005; Webb, 2020). GPR data were collected on 12, 20, and 26 February at the same time as the snow pit data collection (Table 3). A GPR pulse is

Table 3. Snow pit data collected for the UAVSAR time series. ~~Data-Bulk ρ_s and ϵ_s , which is an average of the 10 cm segments, are reported. No ϵ_s was collected at the BA pit. Data were collected on 20 February and not during the 19 February flight date. No BA pit was dug on February 12. Bulk- ρ_s is reported, and no ϵ_s . The 12 February SWE was collected at estimated using of 10 depth measurements around the BA-pit area and the 20 February ρ_s .~~

Pit	Date	UAVSAR start UAVSAR start (HHMM LT)	Pit start Pit start (HHMM LT)	Depth em(cm)	ρ_s kg m⁻³ Bulk ρ_s (kg m ⁻³)	SWE em(cm)	Mean-Bulk ϵ_s
HQ	2/12	0946 MT	1305 MT	78	261	20.3	1.26
HQ	2/20	1010 MT	1156 MT	67	302	20.2	1.39
HQ	2/26	1027 MT	1157 MT	66	309	20.4	1.29
HQ	3/04	H105-MT NA	<u>1105</u>	57	342	19.5	1.56
BA	2/12	0946 MT	NA-1337	NA-82	NA-290	NA-23.8	NA
BA	2/20	1010 MT	1224 MT	80	290	23.2	NA
BA	2/26	1027 MT	1139 MT	82	290	23.8	NA
BA	3/04	H116-MT NA	<u>1116</u>	76	307	23.3	NA

an electromagnetic wave that travels through the snowpack and is reflected off ~~changes in material interfaces between materials with different dielectric~~ properties such as ρ_s , with the strongest reflection often from the snow-soil interface at L-band (Bradford et al., 2009; Holbrook et al., 2016; Webb, 2017). For this study, two-way ~~traveltime~~ travel time (t_2) of GPR waves through ~~snow were the snow was~~ obtained along transects. ~~We used using~~ a Mala Geoscience, Inc. ProEx control unit pulse GPR system with an 800 MHz shielded antenna. The antenna was fixed in place on a plastic sled towed behind the operator. A GPS antenna connected to the ProEx control unit registered location information every second.

Radar pulses were triggered on 0.05 s intervals using eight times stacking (i.e., ~~eight signals collected per point and averaged~~). The average survey travel speed was ~ 0.5 m s⁻¹ resulting in ~~~40~40~~ returns per meter. The ReflexW 2D Software package (Sandmeier, 2022) was used for ~~time-zero adjustment, taken as the first break in the first wavelet and a dewow filter and spherical divergence correction to compensate time-zero adjustment, removing low-frequency background energy (i.e., dewow), and correcting~~ for signal attenuation. ~~The dewow filter removes low frequency content by calculating a running mean that is subtracted from a central point. The reflection of through the snow. For further details of GPR processing methods applied to snow, see Bonnell et al. (2021), McGrath et al. (2019), and Webb et al. (2018). The radar reflection from the snow-soil interface was then selected at the first break prior to the first peak of the reflection. Topographic-A topographic~~ correction was performed by dividing t_2 by the cosine of the ground surface slope at that location.

The ϵ_s of snow is sensitive to ρ_s and LWC (Bradford et al., 2009; Heilig et al., 2015; Webb et al., 2018), and is related to the velocity (v) of the radar wave through snow:

$$v = \frac{s}{\sqrt{\epsilon_s}} \quad (3)$$

where s is the speed of light in a vacuum ($\sim 0.3 \text{ m ns}^{-1}$). For this study, the ϵ_s was directly ~~observed-measured~~ in snow pit observations using an A2 Photonics WISe instrument ~~at 10 cm vertical increments for the entirety of the snow pit height. We then averaged all WISe ϵ_s pit observations as the bulk ϵ_s value (Table 3).~~ The observed ϵ_s was then used to estimate a velocity to distribute snow depth estimates along GPR transects.

$$d_s = \frac{vt_2}{2} \quad (4)$$

These depth estimates were then converted to SWE by multiplying snow depth by the pit-observed bulk ρ_s for direct comparison to ~~UAVSAR-derived-UAVSAR-derived~~ ΔSWE (described further in Section 2.6). When using this approach of GPR observations in combination with a pit-observed bulk ρ_s , we ~~can~~ expect to observe SWE values within 5 % at the frequency used (Marshall et al., 2005). We calibrated our GPR ΔSWE data to the observed ΔSWE at the snow pit. To do this, we defined a bias as the observed mean ΔSWE difference between all GPR observations within 20 m of the snow pit and the SWE measured at the pit. We then removed this bias from the entire GPR dataset to create a directly comparable dataset relative to the ~~UAVSAR-derived-UAVSAR-derived~~ ΔSWE . This is a similar method as described below to ~~tether-tie~~ the UAVSAR data to snow pit observations. ~~The point-based GPR returns were rasterized to the 6 m UAVSAR resolution and only those pixels with 30 or more GPR point observations were retained.~~

2.4 InSAR Atmospheric Correction

~~Radar-While radar~~ signals can penetrate a moist and cloudy atmosphere, ~~but the~~ variation in dielectric properties between wet and dry air can significantly affect the radar signal (Ferretti et al., 2001). While substantial research has been conducted for correcting both tropospheric ~~and-ionospheric~~ (Yu et al., 2018) and ~~ionospheric~~ (Meyer, 2011) effects from satellite-based SAR (Meyer, 2011; Yu et al., 2018), suborbital SAR is both less common and has different correction considerations due to the lower acquisition altitude and often shallower and more diverse observation geometries. ~~However in one recent study, Michaelides et al. (2021) laid out an approach to successfully corrected UAVSAR atmospheric delay using a high-pass and low-pass filtering sequence.~~

Tropospheric atmospheric delay effects can be divided into two parts ~~the~~ dry delay and ~~the~~ wet delay. The dry delay is caused by variations in temperature and pressure and is often considered less significant than the wet delay for spaceborne ~~sensing applications~~ (Zebker et al., 1997). Wet delay is caused by spatial (within swath) and temporal (between acquisitions) variations in atmospheric water vapor concentrations (Danklmayer et al., 2009). ~~Two recent studies (Michaelides et al., 2021; Bekaert et al., 2021) developed unique approaches to correct UAVSAR atmospheric delay. However, these methods were not directly applicable to the type of delay seen in our UAVSAR data.~~

As seen in Figure 4a, ~~the raw 6a, the 12-19 February uncorrected~~ unwrapped phase data shows a noticeable near-to-far range phase ramp. For this UAVSAR flight, the average altitude was 12.9 km, compared to a satellite that traditionally orbits ~~around 750 at ~750~~ km. This vastly lower sensing altitude causes a larger diversity of look angles and radar ~~path-look vector~~ length variations between the near and far ranges of the radar swath to emerge. The radar ~~path-length-vector (PLV)~~ ~~slant range~~, or the

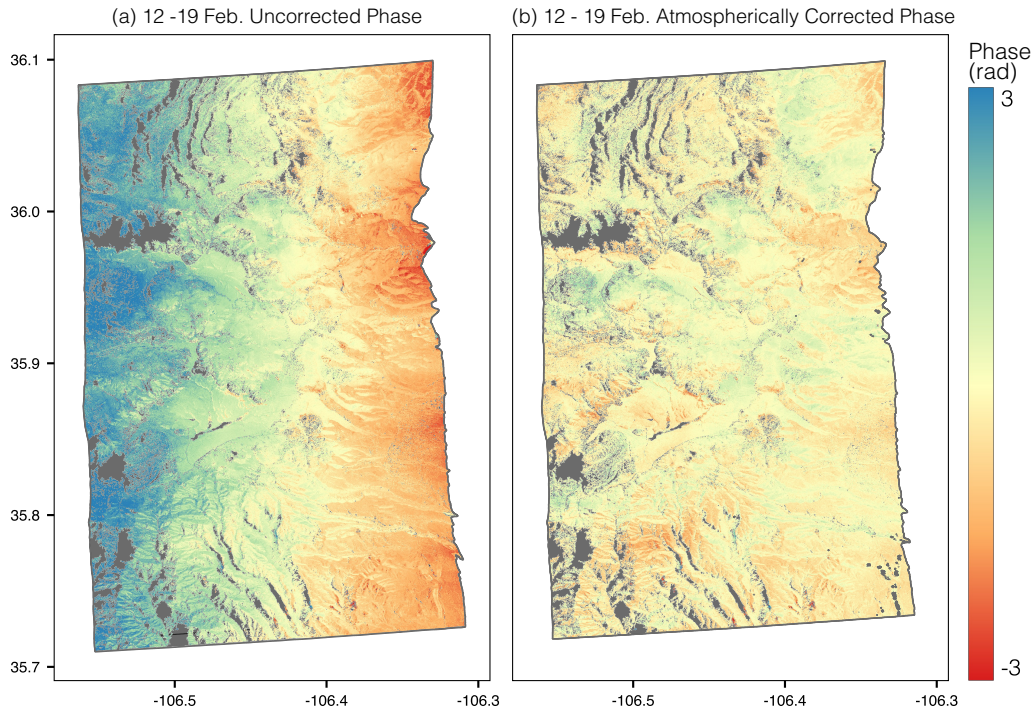


Figure 6. (a) Shows the The uncorrected unwrapped phase from the 12-19-12-19 February pair and (b) the atmospherically corrected phase data. There is a linear ramp in the phase that is linearly increasing phase ramp from near-to-far range (east to west), which is a distance of approximately 22-22 km. (b) Shows the atmospherically corrected phase change data.

distance between a point on the ground and the radar, ranged between spanned from 11.4km and 27.8 km-27.8 km. The look angle varied from 28.51° in the near range to 69.01° in the far range. Thus, the radar wave in the far range is traveling through more atmosphere than the near range by a factor of 2.4.

Assuming a spatially homogeneous change in atmosphere between acquisitions, we developed a method to correct for the phase ramp by calculating the distance from the radar to a point on the ground for every pixel in the scene, also known as the path length vector (PLV). The PLV used the pixel-wise slant range distance, or radar look vector (LKV), to correct the phase ramp. LKV is mostly dependent on the near-to-far near-to-far range position in the scene \vec{r} , but also varies with local topography. PLV-LKV is calculated by geocoding the easting-east (e), northing-north (n), and up (u) components of the SLC data: single look complex (SLC) .lkv file (Supplement). The distance is then calculated by summing these components in quadrature:

$$315 \quad \underline{PLV LKV} = \sqrt{e^2 + n^2 + u^2} \quad (5)$$

Embedded within the atmospheric delay phase signal is the smaller scale snowpack variation phase signal. By only Phase values can be impacted by atmospheric delay and snowpack fluctuations simultaneously. By calculating the atmospheric delay

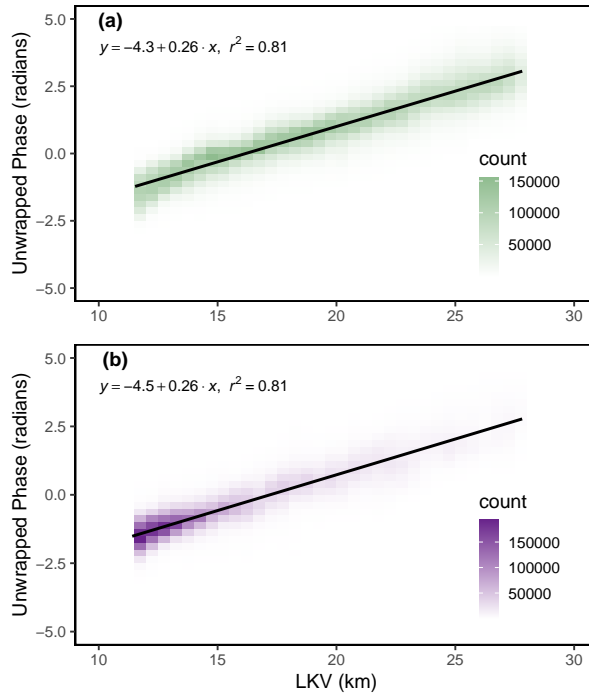


Figure 7. Density scatter plots showing the relationship between unwrapped phase and LKV in the radar PLV for the 12-19-12-19 February InSAR pair for (a) snow covered pixels and (b) snow free pixels. The similarity in the two plots shows the large-scale-large-scale phase signal is atmospheric and not snowpack related.

of only snow free pixels from the Landsat fSCA product on defined by the 18 February fSCA product for the whole UAVSAR swath and comparing it to the atmospheric delay of only snow covered pixels, we were able to confirm the bulk of the observed
 320 signal is atmospheric and not snowpack-related (Figure 5b snowpack related (Figure 7b)). Using data from meteorological stations, we know there was not a large-scale-large-scale snowfall event between the two flights. Using the linear relationship ($r^2 = .81$) between PLV 0.81) between LKV and phase shown in Figure 5a7a, we subtract the estimated atmospheric component from the raw uncorrected data to achieve the atmospherically corrected image (Figure 4b6b). This correction was also applied to 12-26 February pair as it showed the same atmospheric delay method was applied to the 12-19 February and 12-26 February
 325 pairs.

2.5 Generating Local Incidence Angle Data

The local incidence angle-angle (θ) angle is the angle between the ground surface normal and the radar line of sight calculated LKV on a per-pixel basis (Figure 1). The angle is calculated by deriving the surface normal from a DEM and computing the dot product with radar path length vector the LKV:

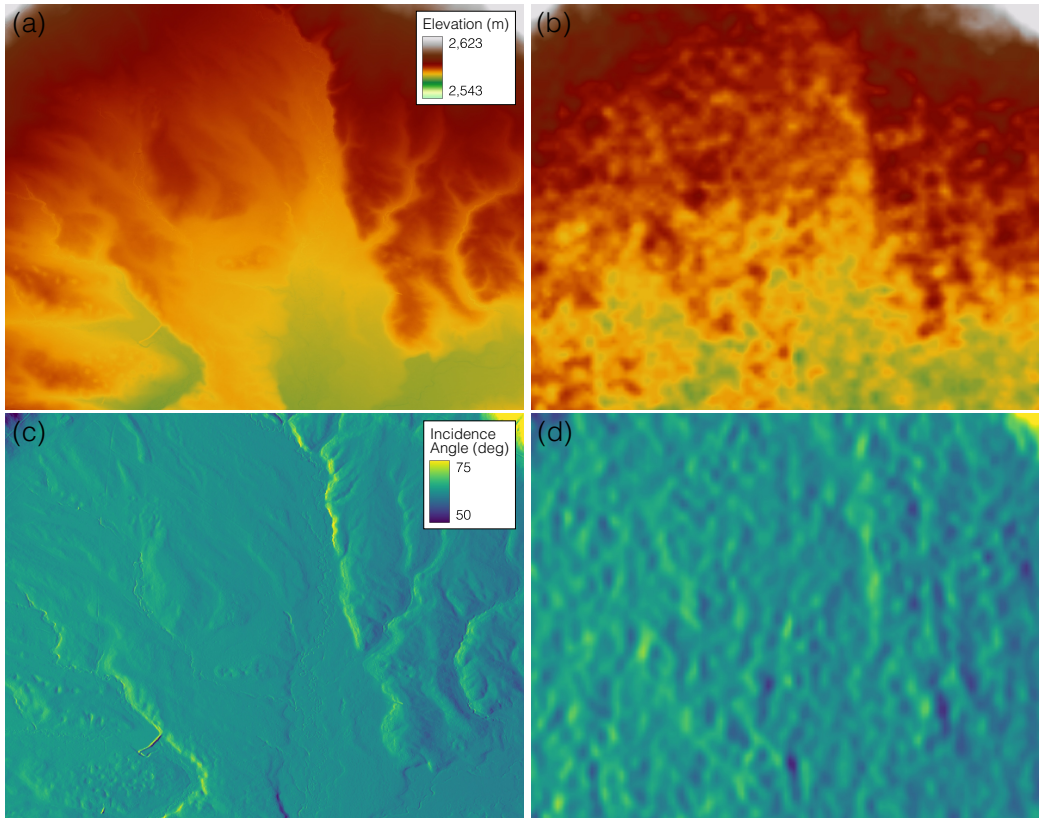


Figure 8. The snow free ground surface and UAVSAR θ in a portion of the VG meadow for (a) the lidar DEM and (b) the new SRTM DEM. UAVSAR θ data is generated from the lidar DEM (c) the JPL SRTM DEM lidar and (d) the θ SRTM data provided by JPL. Gullies and small stream channels are easily discerned from the lidar data DEM, while the SRTM DEM shows a variable surface with large undulating mounds.

$$330 \quad \theta = \cos^{-1}(-\hat{n} \cdot \underline{PLVLKV}) \quad (6)$$

Where θ is the local incidence angle, \hat{n} is the surface normal, and PLV is the radar line of site vector length. θ varies with respect to local topography and the PLVLKV. θ affects the distance the radar wave will travel through the snowpack and is a direct input into the SWE change inversion algorithm (Equation 2). We found significant errors within the original SRTM DEM used in the UAVSAR data processing (Figure 6e). The meadow in Valle Grande is 8b). This error is likely due to phase noise in the SRTM interferograms as it is consistent throughout the dataset and falls within the known SRTM vertical uncertainty of ± 16 m (Rodríguez et al., 2006; Sun et al., 2003). VG is relatively flat and smooth outside of river channels and gullies. However, the original DEM shows mounds and undulations artifacts on the order of 10 to 20 5–15 m throughout the meadow that do and does not accurately represent the ground surface. These DEM errors artifacts propagate into the estimate of θ (Figure 6d8d), which is then input into the SWE change equation, causing errors in SWE change estimations.

340 The original DEM used in interferometric processing is an SRTM 30 m product that had been downsampled to the native
UAVSAR resolution of 6 m. The Spaceborne Imaging Radar-C/X-band Synthetic Aperture Radar (SIR-C/X-SAR) acquired the
single-pass interferometric from the Space Shuttle Endeavor in February 2000. During the midwinter acquisition period, snow
cover was present at our study site. Radar waves a C-band can penetrate dry snow up to several meters, but the presence of
liquid water changes the dielectric and scattering properties of the snowpack (Farr et al., 2007), influencing penetration depth,
345 and likely caused the observed issues with the initial DEM.

We generated new θ data using a snow free lidar DEM (Figure 6a8a) acquired in 2010 for the Catalina-Jemez Critical Zone
Observatory (CZO) (OpenTopography, 2012). The high spatial resolution (of 1 m) and lack of interference from snow provide
and elevation accuracy of 5–30 cm provides a more reliable starting point to calculate θ . By using the PLV-LKV and the lidar
DEM, the new θ data better represent the bare ground surface of VG (Figure 6b8c).

350 2.6 Calculating SWE Change

To begin the SWE change estimation, the three InSAR pairs were masked with Landsat fSCA data collected on 18 February
2020. All pixels with > 15 % snow cover were included to not mistakenly exclude pixels in the forest where the snowpack is
partially obstructed by forest canopy. Using Equation 2, Δ SWE values were calculated on a pixel-wise basis with inputs of λ_i
(23.84 cm), ρ_s , ϵ_s , and the lidar-derived lidar-derived θ . ρ_s and ϵ_s are averages of the two snow pit values (Table 2) between
355 the two acquisition dates.

InSAR phase differences produce a relative measurement of change in SWE, therefore this-these data need to be tethered
tied to a point on the ground to estimate absolute change. Since there was near zero SWE change at the HQ snow pit between
the three UAVSAR acquisitions (Table 23), we used this location as our InSAR known change point. This SWE change of -1
cm for 12-19 February and -2 cm for 19-26 -0.1 cm for 12-19 February and 0.2 cm for 19-26 February is well within the
360 margin of measurement error (10 %) for the snow pit observations. To account for error within both-GPS snow pit location and
the geocoding of the InSAR data, the Δ SWE values for the snow pit pixel and the eight surrounding pixels were averaged and
this. This averaged value was subtracted to obtain an absolute change. To calculate the cumulative Δ SWE, the 12-19 February
and 19-26 February two 7-day pairs were masked so only pixels that occurred in both scenes were considered , and then added
together.

365 3 Results

3.1 InSAR Polarization, Unwrapped Phase, and Coherence Δ SWE

UAVSAR unwrapped phase (UNW) and coherence statistics for the full scene (FS) and Valle Grande (VG). UNW Loss % is
the percentage of pixels lost in the unwrapping process. Pair Polarization FS Mean Coherence VG Mean Coherence FS UNW
Loss % VG UNW Loss % 12-19 Feb. HH .53 .50 9.4 7.7 12-19 Feb. HV .44 .34 17.7 42.0 12-19 Feb. VH .44 .36 23.7 56.9

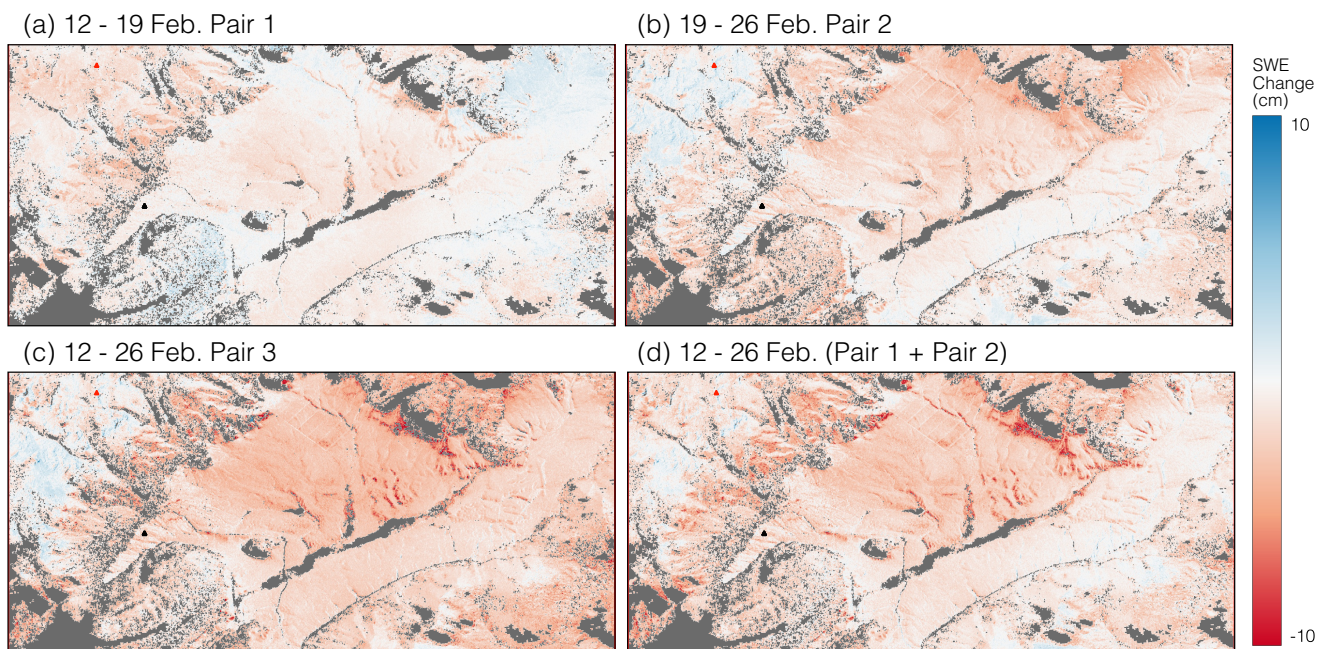


Figure 9. The atmospherically corrected unwrapped phase and coherence data InSAR-derived Δ SWE results for the (a) 12-19-12-19 February, (b) 19-26-19-26 February, (c) 12-26-12-26 February InSAR pairs, and (d) and the amplitude data for cumulative change between 12-26 February generated by adding the three UAVSAR flights. The grey area in the phase data are pixels lost in in the unwrapping processes from (a) and (b) together. The VG meadow and Jemez River main channel are outlined by blue and triangles represent the BA (reddotted lines respectively) and HQ (black) snow pits.

370 12-19 Feb. VV .54 .50 8.9 12.8 19-26 Feb. HH .55 .52 5.0 4.1 19-26 Feb. HV .49 .38 8.2 10.7 19-26 Feb. VH .47 .37 11.8 17.4
 19-26 Feb. VV .57 .54 4.3 3.7

Three interferometric products – coherence, unwrapped phase, and the interferogram are produced for every InSAR pair. Coherence measures the consistency of the scattering characteristics within a pixel between InSAR acquisitions. Unwrapped phase is the estimated absolute phase change in a pixel, generated from the initially ambiguous interferogram, which is defined modulo 2π .

380 When there is a significant change in the landscape scattering properties between InSAR acquisitions, phase noise and fringe discontinuities increase, coherence decreases, and the unwrapping algorithm performs less reliably (Balzter, 2001). We analyzed the coherence and unwrapped phase products for all four polarizations to assess their quality before implementing the SWE change equation. We found co-polarizations (HH & VV) to have the highest average coherence and the greatest percentage of pixels preserved in the unwrapping process (Table 3) compared to cross-polarizations (VH & HV). We choose to analyze HH and only processed this polarization for the 12-26 February pair with ISCE2.

The right side of Figure 7 shows the coherence values in VG for the InSAR Δ SWE results are displayed in Figure 9 for (a) 12-19 February, (b) 19-26 February, and (c) 12-26 February. In the coherence maps there are clear patterns with respect to topography and probable variations in snowpack LWC. The area of lowest coherence surrounds the main channel of the Jemez River (red dotted line) that flows through the south-central portion of VG. As seen in Figure 7d there is a variable area of low backscatter in all three amplitude images. This backscatter decrease is likely caused by snowpack LWC attenuating the radar signal. The spatial variability in LWC between acquisitions causes low coherence and the loss of pixels in the unwrapping processes for all three pairs in this riparian area. There are also horizontal streaks of low coherence and high backscatter within the images, likely a result of artifacts from the InSAR and SAR processing. These lines do not propagate into the unwrapped phase data and therefore are not of significant concern.

The left side of Figures 7a, 7b, & 7c show the unwrapped phase values for InSAR pairs. In the open meadow (blue dotted line), the unwrapping algorithm performs well, and most pixels are persevered except in the riparian area for the reasons described previously. The other primary source of low coherence and corresponding unwrapping pixel loss occurs on the forested hill slopes surrounding the VG meadow. Overall, the unwrapped data provides a high quality input into the SWE change inversion equation.

3.2 Mapping Changes in SWE

Figure 8 shows (d) 12-26 February cumulative change (CM) in the study area. Table 4 reports Δ SWE results for 12-19 February, 19-26 February, 12-26 February, and the cumulative change between 12-26 February in VG. In SWE mean, standard deviation (SD), median, interquartile range (IQR), and is split into four physiographic classes. First is the full study area (Figure 8a (12-19 2d), followed by the three defined in Figure 2f: VG, north facing slopes, and south facing slopes. Figure 10 shows histograms of InSAR-derived Δ SWE for the four aforementioned classes. We note that there was a greater mean estimated SWE loss for 19-26 February compared with 12-19 February for all physiographic regions (Figure 10a-d).

In Figure 9a (12-19 February), the full study area has a mean change of -0.52 Δ SWE of -0.52 cm, with much of the VG meadow showing similar change. The 99th and 1st percentile of the Δ SWE data are reported in Table 4. In the meadow the VG showing a similar change of -0.62 cm. In VG, the largest SWE losses occur on the south aspect slopes around in gullies and terrain depressions, with these areas showing visible SWE loss in all four pairs. The northeast corner of the study area shows a consistent increase in SWE, on the order of less than a centimeter. While there are more pixels lost on the forested hill slopes, there < 1 cm. There is a pattern of more SWE loss on the south facing slopes (mean = -0.58 cm) than the north facing, which would make sense for melt impacts at this time of year. (mean = -0.24 cm) for this pair.

Figure 8b (19-26 February), 9b (19-26 February) displays similar spatial patterns to the first pair those of Figure 9a. Overall the mean SWE loss was -1.24 cm for this time frame -1.24 cm, with the same gully areas showing the greatest loss. VG losing on average -1.34 cm. These SWE losses are over double that of 12-19 February. The highest elevation occurs in the northwest corner of the scene near Redondo Peak, and it is the only place to show consistent SWE increases. These increases compared well are compared with in situ snow depth sensors SWE data in the area (see Section 3.4.3.2). The pattern between of more than double the SWE loss on south aspect slopes and a constant to slight gain of SWE on north aspect remains facing slopes

(mean = -1.45 cm) compared to north facing (mean = -0.75 cm) continues from the first pair, with the small storm explaining north aspect increases.

Figure 8e (12-26 February) is the only pair not processed by the UAVSAR team. It had The 14-day baseline pair, 12-26 February (Figure 9c), has a mean Δ SWE of -2.67 cm. The cumulative Δ SWE (Figure 8d) map was -2.29 cm. 12-26 February CM (Figure 9d), created by adding the values of Figure 8a and 8e together. The 9a and 9b together, has a mean value of the cumulative SWE change was -1.76 cm, with a range of 1.51 to -6.8 cm. The -1.70 cm. While the IQR, SD, and histogram shape (Figure 10d-h) are similar in all four physiographic sections of the 14-day data, the mean of 12-26 February has a negative bias of ~0.5 cm compared to 12-26 February CM. This is likely due to variations in how these data were atmospherically corrected. The spatial patterns observed in the individual two 7-day InSAR pairs become more evident in the both Figure 8e & 8d, with the greatest losses (3-6 cm) occurring in the gullies of the VG meadow and the south facing forested hill slopes above. amplified in both Figure 9a compares the distribution of SWE change values for the 12-19 and 19-26 February pairs, and Figure 9b 9c and 9d.

As a first-order estimate of uncertainty within the technique, we calculated the Δ SWE values for 12-26 and cumulative 12-26 February pairs. 19-26 February shows more SWE loss than 12-19 February areas considered snow free by the 18 February fSCA data (Figure 4d). The Δ SWE data from the three pairs (12-19, 19-26, and 12-26 February) were combined, and we report a snow free Δ SWE mean value of -2.06 cm, an SD of 1.56 cm, and an IQR of 2.14 cm.

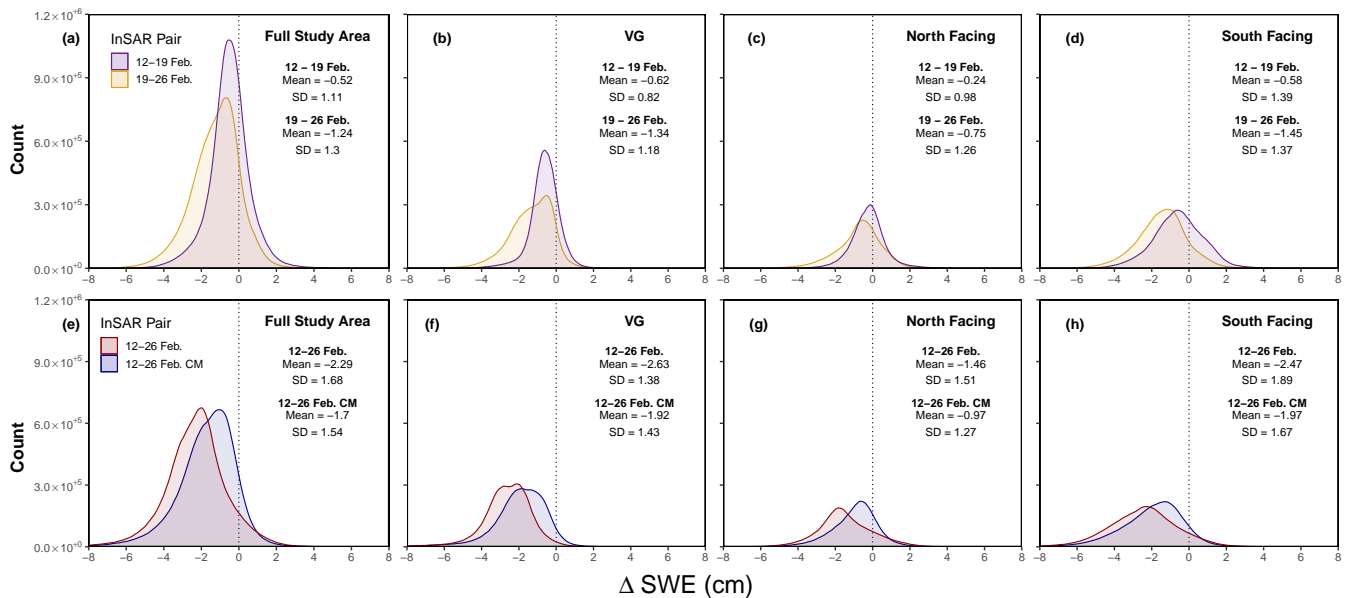


Figure 10. InSAR-derived The distribution of Δ SWE results values for (a) 12-19 the full study area, within VG, north facing, and south facing slopes. The top row displays the 12-19 and 12-26 February InSAR pairs (ba-d) 19-26 February (e) 12-26 February (d), and the cumulative change between 12-26 February generated by adding bottom row shows the data from (a) 12-26 and 12-26 CM February InSAR pairs (bd-h) together.

Table 4. Δ SWE summary statistics (cm) mean, SD, median, and IQR from Figure 8 in cm9 for the four InSAR pairs analyzed. 12-26 They are split into the same four physiographic classes (full study area, VG, north facing slopes, and south facing slopes) as Figure 10. 12-26 February cumulative (CM) is created by adding the SWE changes from 12-19-12-19 February and 19-26-19-26 February pairs.

InSAR Pair	Δ SWE (cm)			
	Δ SWE Mean	Δ SWE 99th% SD	Δ SWE 1st% Median	Δ SWE SD IQR
<u>Full Study Area</u>				
12-19-12-19 Feb.	-0.52-0.52	2.34-1.11	-3.63-0.50	1.11-1.18
19-26-19-26 Feb.	-1.24-1.24	1.61-1.30	-4.80-1.12	1.30-1.64
12-26-12-26 Feb.	-2.67-2.29	2.07-1.68	-8.79-2.24	2.02-1.87
12-26-12-26 Feb. CM	-1.76-1.70	1.54	-1.53	1.86
<u>VG</u>				
12-19 Feb.	-0.62	0.82	-0.59	0.88
19-26 Feb.	-1.34	1.18	-1.20	1.56
12-26 Feb.	-2.63	1.38	-2.53	1.54
12-26 Feb. CM	-1.92	1.43	-1.78	1.66
<u>North Facing Slopes</u>				
12-19 Feb.	-0.24	0.98	-0.23	1.04
19-26 Feb.	-0.75	1.26	-0.62	1.45
12-26 Feb.	-1.46	1.51	-6.80-1.58	1.62-1.78
12-26 Feb. CM	-0.97	1.27	-0.83	1.47
<u>South Facing Slopes</u>				
12-19 Feb.	-0.58	1.39	-0.58	1.74
19-26 Feb.	-1.45	1.37	-1.39	1.67
12-26 Feb.	-2.47	1.89	-2.42	2.33
12-26 Feb. CM	-1.97	1.67	-1.78	2.08

Histograms displaying the distribution of Δ SWE values for (a) 12-19 February and 19-26 February, and (b) 12-26 February and the cumulative change between 12-26 February.

3.2 InSAR vs. Snow Depth Sensors, Snow Pits, and GPR Δ SWE

435 3.3 Changes in SWE: InSAR vs. GPR

We compared the Δ SWE InSAR results to GPR data collected between 12-26 February. The point GPR returns were rasterized to the 6 m UAVSAR resolution where only pixels with 30 or more GPR point observations were retained ($n = 129$). Figure 10 is a scatter plot of the 12-26 February and 12-26 February cumulative change (12-19 + 19-26 February) InSAR pairs compared with the GPR. The InSAR-derived SWE retrievals were compared to three types of in situ SWE data: snow depth sensors, snow pits, and GPR. Figure 11a is a plot of Δ SWE returns from the same time period. While no significant relationship was found, there is a relatively small difference in average values from the six CZO snow depth sensors and BA pit (~3030 m), and HQ Met snow depth sensor and pit (2650 m) against the InSAR Δ SWE from the two methods. It can be seen that the GPR observations center near a Δ SWE value of zero (mean of -0.17 cm) and SWE values. Due to many of the in situ measurements being on or near the edge of a pixel, the InSAR-derived InSAR Δ SWE shows slightly more negative values with a mean value of -2.34 cm.

Both of these methods were calibrated using the previously mentioned HQ snow pit and thus, this comparison shows a slight negative bias (loss of SWE) on the order of ~2 cm for the InSAR method for the conditions of this study. However, this likely represents a maximum error due to the five percent uncertainty of the GPR method, or ~1 cm SWE for each observation date, and therefore 1-2 cm for the GPR Δ SWE product. Additionally, the difference in timing between the UAVSAR overflight and the GPR survey of about three hours could have resulted in an increase of LWC in values are an average of the pixel in which the measurement falls and the snowpack during the GPR survey, and therefore an underestimate of SWE loss, although this is likely minimal due to the re-freezing of the snow surface overnight and observed HQ pit temperatures. Thus, the observed InSAR Δ SWE difference of ~2cm relative to GPR observations provides an estimate of InSAR Δ SWE retrievals.

Scatter plot comparing InSAR and GPR derived Δ SWE for the 12-26 February and 12-26 cumulative pairs.

3.3 Comparison to In-Situ Snow Depth Sensors

We compared seven in situ snow depth sensors to InSAR-derived SWE changes. Figure 11 is a time series of snow depths from seven ultrasonic sensors from 12-26 February. Six of sensors are located on Redondo Peak and one is on the HQ Met station in VG. The grey shaded area on the plot shows a four closest pixels. The InSAR retrievals had a root mean square error (RMSE) of 1.46 cm and an MAE of 1.16 cm compared to the in situ measurements ($n = 27$, $r^2 = 0.34$). The small snowfall event starting the night of 22 February and ending 23 February. This snowfall is only noted in Section 2.3.3 is registered in the higher elevation sensors and CZO sensors and BA pit and not in the HQ Met location (Figure 5a). We see this same pattern for InSAR-based returns in Figure 8b (19-26 February). VG 9b (19-26 February), which is also shown by the mostly positive values of the pink dots in Figure 11a. The study area shows mostly SWE loss, while the higher elevation area in the northwest corner of the plot shows an area of increase, which is captured by the in situ sensors, increase indicating general agreement in the ablation and accumulation patterns.

In situ snow depths were converted to SWE by multiplying by the bulk ρ_s of 290 kg m^{-3} (from snow pit observations) for the three pairs when there was We compared the InSAR and GPR Δ SWE between 12-26 February (Figure 11b). No significant relationship was found ($r^2 = .042$), and the RMSE and MAE increased to 3.03 cm and 2.57 cm, respectively. The error metrics were calculated using the GPR data as validation, yet offsets in acquisition timing between UAVSAR and the GPR likely

470 caused increased uncertainty when comparing the two datasets. On 12 February, the GPR acquisition began ~3 h after the 0946
LT UAVSAR flight, and on 26 February, the GPR data collection started ~2 h after the 1027 LT UAVSAR acquisition. During
these acquisition time offsets, both temperature (Figure 5b) and incoming solar radiation (Figure 5d) were increasing. These
atmospheric conditions presumably led to increases in snowpack LWC and ϵ_s , which would explain why 44% of the GPR
 Δ SWE values showed increases when no measurable snowfall occurred in VG during the study period. We note that the presence of liquid water in the snowpack
475 interval board for the 19-26 February pair. These SWE measurements were compared against the InSAR pixel's they're located
in Figure 12 ($n = 28, r^2 = .3$)
can cause a GPR signal delay that could be incorrectly interpreted as an increase in SWE. However, it should be stated that
many of these points remain within the known uncertainty (± 1 cm SWE) of L-band GPR observations for a dry snowpack
(McGrath et al., 2019), with higher uncertainty expected during wet snow conditions. Furthermore, the mean GPR derived
480 Δ SWE product is ~0 cm, which matches well with the pit-observed change of ~0 cm (Table 3). The InSAR-derived Δ SWE
product has a mean of -2.63 cm in VG; this indicates potential differences arise from using the pit observed ϵ_s measurements
occurring later in the day than the InSAR retrievals and at the same time as the GPR survey. The potential change in snowpack
properties that can occur during this time, as previously mentioned, could further explain these differences between the GPR
and InSAR-derived products. However, it is important to note that these differences of 2-3 cm remain small in the context of
485 other remote sensing techniques, especially when considering complex spring snowmelt conditions.

Comparing in-situ SWE changes from the six CZO and the HQ met snow depth sensors to InSAR-derived SWE changes
for four InSAR pairs. Snow depths are converted to SWE by multiplying by ρ_s from the BA snow pit. The in-situ SWE error
bars represent a 10% uncertainty from the snow pit density measurements and 2 cm uncertainty from the ultrasonic snow depth
sensors.

490 3.3 Δ fSCA vs. InSAR Δ SWE

We compared the InSAR Δ SWE from 12-26-19-26 February (Figure 13a12a) to Δ fSCA between 18 February and 5 March
(Figure 13b12b). The InSAR data was/were aggregated up to the 30 m Landsat resolution. While these datasets measure two
different variables (SWE vs. fSCA) during different acquisition periods, the comparison of snow ablation patterns provides
(fSCA reductions) patterns provide useful information when attempting to validate the experimental InSAR results.

495 Several landscape features are prevalent in both datasets. The long gully that runs from the north central area of VG to the
Jemez River is shown clearly in both maps. Other smaller gully's-gullies are also clearly visible. There are both SWE and fSCA
losses on the the south facing hillslopes surrounding the VG. Both of these patterns are being driven by these areas receiving
more direct solar radiation. In the northwest corner of the image, the InSAR-derived map shows a small area of SWE increase,
and the fSCA image shows no loss in this area.

500 Limited complete fSCA loss occurred in much of VG meadow, while 1-3 cm losses in SWE were recorded throughout the
whole meadow, while a mean value of -1.34 cm SWE was recorded. For optical images to show fSCA loss, bare ground must
appear in the pixel. For the majority of the snow melt season, pixels lose SWE while still being completely snow covered. The
fSCA product also shows more areas of melt than the Δ SWE product, which can be explained by the eight day difference in

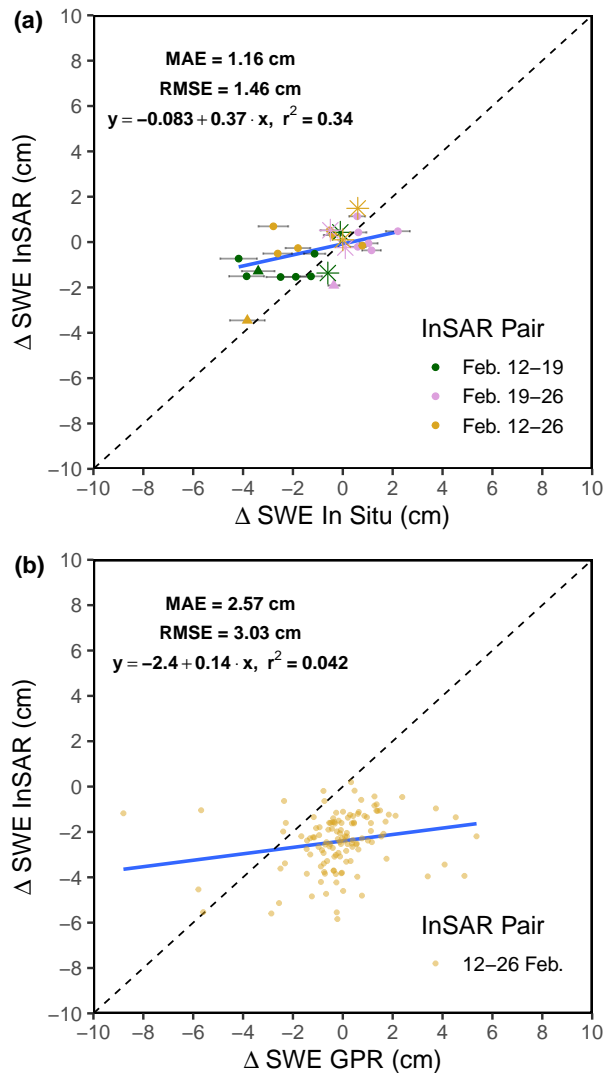


Figure 11. A snow depth time-series for (a) Comparing in situ SWE changes from the six CZO sensors (beginning with DS circles) on Redondo peak, HQ snow depth sensor (triangles), and the BA and HQ met-sensor-pits (red stars) at a lower elevation in VG to InSAR-derived SWE changes for the three InSAR pairs. All six of The depth sensor SWE error bars are derived from a 10 % uncertainty from snow pit ρ_s measurements and ± 1 cm uncertainty from the higher elevation CZO ultrasonic depth sensors show precipitation event starting on 22 February. (grey shading b), while the HQ sensor does not Comparing InSAR and GPR derived Δ SWE from 12–26 February.

505 attributed to the eight-day difference in the date of the last acquisition (26 February vs. 5 March). During that eight day period the field teams noted that melt started to progress at a higher rate which, and areas of the meadow became bare seen in both the fSCA imagery and by field teams On 4 March, field teams reported widespread snowmelt throughout VG and the emergence of bare ground. The optical data also show areas of 100 % fSCA reduction and, therefore, bare ground appearing. fSCA gains are

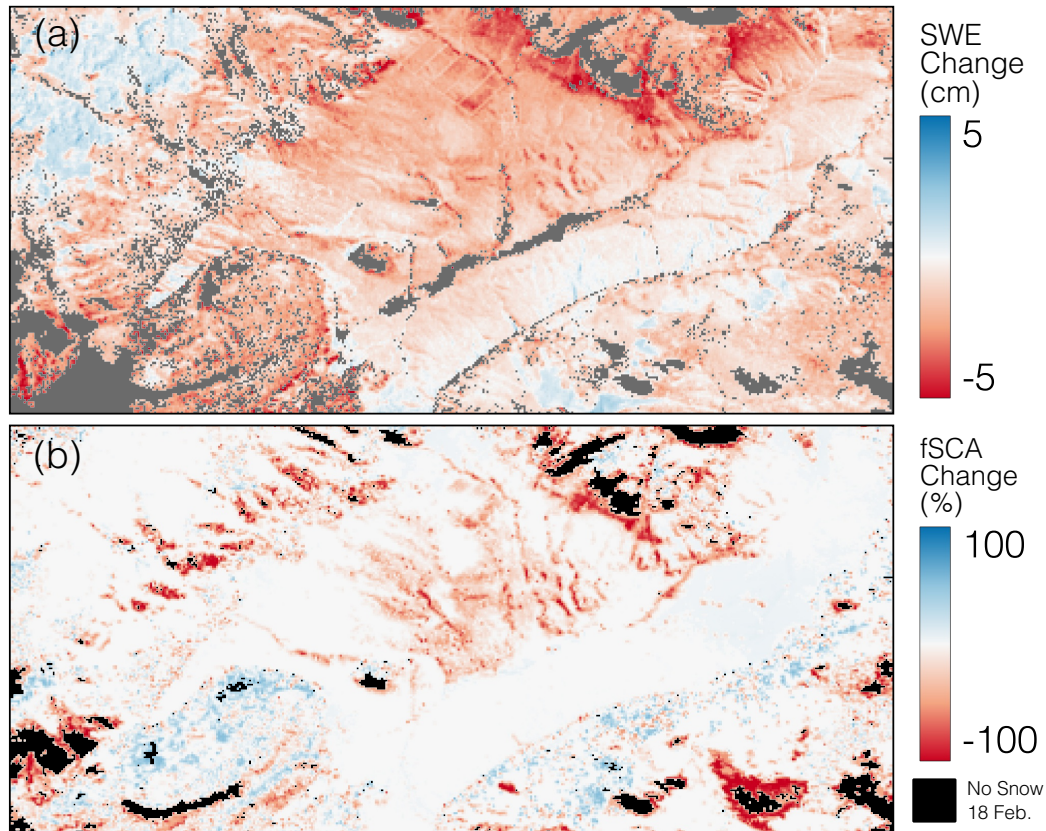


Figure 12. (a) ~~The cumulative InSAR-derived InSAR~~ Δ SWE between ~~12-26-19-26~~ February ~~resampled up aggregated~~ to the ~~Landsat resolution of 30 m Landsat resolution~~, and (b) the ~~change in~~ Landsat Δ fSCA between 18 February and 5 March. ~~The color scale for (a) was changed to -5 to 5 cm to exemplify the patterns.~~

recorded in the ~~forested areas densely forested hillslopes~~ south of VG. ~~This uncertainty arises~~, which are shown by the true color imagery (Figure 4g and 4h). ~~Uncertainty arises in forested areas~~ from how the fSCA algorithm deals with sub-canopy forest snow estimation.

4 Discussion

4.1 Key Findings

During the study ~~time frame period~~, there was one localized measurable precipitation event on Redondo Peak, and temperatures were diurnally fluctuating below and above freezing ~~during the study period (Figure 14(Figure 5b))~~. With the snowpack going through daily partial freeze-thaw cycles, creating large sintered grains, and average wind speeds of 2.4 m s^{-1} (Figure 5c), there is a low probability of blowing snow being a significant driver of SWE loss. ~~This is further confirmed by observations from~~

~~the field team that~~ Field team observations noted the hard surface of the snowpack during this time. This means that incoming solar radiation, causing surface melt and sublimation during the day, ~~is was~~ the likely primary driver of ~~measured~~ SWE loss. ~~According to our data, the greatest SWE losses occurred in gullies in VG and on south aspect slopes of the surrounding forested hillslopes. These are also the areas that~~ This is further confirmed by south facing slopes, which receive the most direct incoming solar radiation. ~~This finding aligns, showing about double the amount of SWE loss to that of north facing slopes for all InSAR pairs. These findings align~~ with work by Musselman et al. (2008), who also observed midwinter SWE loss driven by incoming solar radiation in VCNP.

We hypothesize that the snowpack would become partially isothermal during the day ~~and~~, start to melt, and the surface would refreeze at night. The three UAVSAR flights occurred between ~~9:30-10:30 AM~~ 0930-1030 LT when the snowpack was still mostly frozen, allowing the radar signal to hold coherence even though ~~some minimal~~ LWC was still likely present in the snowpack (Webb et al., 2021a). ~~While the pit data noted minor melting for both the 20 and 26 February pits, it is important to clarify that the snow pits were collected 3 hours after the radar data acquisition. This confirms the findings of Bonnell et al. (2021), suggesting that during the melt season where there is still a freeze-thaw diurnal pattern, the 6:00 AM acquisition timing could hold coherence well enough to track snow that had melted during the day and refrozen over night.~~ For SWE loss to occur with this hypothesis, melted snow needs to exit the snowpack or flow downslope. If melted snow is moving through the entire snowpack, it will not be entirely refrozen based on the meteorological data. It is possible that lateral flow within the snowpack (Eiriksson et al., 2013; Evans et al., 2016) (Webb et al., 2021a; Eiriksson et al., 2013; Evans et al., 2016) is moving snowmelt downslope between acquisitions.

Both the spatial distribution ~~of SWE change patterns and the magnitude of these~~ and magnitude of the Δ SWE patterns make sense, ~~when~~ assuming insolation is the primary mechanism driving SWE change during this time period. These patterns are confirmed by ~~visual~~ visually comparing the Δ SWE to Δ fSCA (Figure ~~13~~ 12). There are noticeable similarities in the areas of greatest loss between the two datasets. The variation in acquisition time period and different parameters being measured do not allow for a direct quantitative comparison. However, when Marshall et al. (2021) quantitatively compared lidar snow depth ~~change~~ changes to the UAVSAR phased-based depth retrievals, they found ~~the overall distribution of depth changes and spatial patterns agreed remarkably well~~ an r^2 of 0.76, an RMSE of 4.7 cm for snow depth, and 0.9 cm for SWE. These results add confidence to the findings presented here. ~~Our GPR data provide further justification in our analysis beyond single point comparisons, and show similar RMSE values to the point-based snow depth sensor and snow pit comparisons presented in Figure 11a (RMSE 1.54 cm SWE).~~

The InSAR Δ SWE retrievals showed a stronger correlation to the snow pit and snow depth sensors Δ SWE compared to GPR. The depth sensors estimated SWE from snow height at a single point location and a bulk ρ_s value from the nearby BA snow pit. GPR is a spatial observation that depends on the snow's dielectric properties, similar to InSAR retrievals. This makes the radar methods for deriving SWE more sensitive to variability in snowpack properties such as density, LWC, and ϵ_s . The GPR survey was conducted during mid-day when LWC can vary significantly as a result of increased solar radiation, which in turn increased the uncertainty in observations (e.g., 44 % of GPR pixels showed increasing SWE). The GPR measured some slight SWE increases, meaning there were increases in ϵ_s ; this is a sign that melt had begun during the afternoon acquisitions. Future GPR

analyses will benefit from validation data collected over larger areas and, synchronous timing with remote sensing acquisitions, and greater SWE variations between acquisitions. We believe GPR is a vital tool for future InSAR SWE validation efforts.

The ~~19-26~~ 19-26 February pair is of particular interest because of the snowfall event (Figure ~~H5a~~ H5a) that occurred on 22 February ~~7~~ in the vicinity of Redondo Peak. This snow accumulation event was detected by the InSAR data, in situ snow depth sensors, and interval boards in the area of the BA snow pit. The lower elevations showed no accumulation in the InSAR retrievals, and this was confirmed by both the HQ met snow depth sensors and snow pit (Figure ~~8b11a~~ 8b11a). These results illustrate the ability to track both snow ablation and accumulation within the same radar swath, furthering our confidence in the ~~techniques~~ technique's ability to measure Δ SWE in a wide range of conditions. It is important to note that these small changes are within what can be an expected range of uncertainty for Δ SWE estimation due to LWC variations impacting the spatial variability of ϵ_s during spring snowmelt; capturing the spatial patterns within this range indicates great promise for future applications.

Leveraging morning acquisitions, we showed the UAVSAR L-band InSAR is able to maintain coherence over a 14-day baseline, even in the presence of diurnal melt cycles. The 12-26 February held coherence and provided quality snow phase information. This further supports the robustness of the technique for NISAR's 12-day repeating orbit. However, the biases between the 12-26 and 12-26 CM pairs, resulting from variations in their atmospheric correct, present additional complications. This is discussed in further detail in Section 4.2.

Corresponding research by Webb et al. (2021b) investigated the relationship between ~~dielectric permittivity~~ dielectric permittivity ϵ_s and LWC for both dry and wet snow conditions in the Jemez Mountains. With ρ_s ranging between 261 to 309 kg m⁻³ and ϵ_s between 1.26 to 1.39, snowpack LWC would range approximately between ~~3% to 5%~~ 3-5 %. This validates figures presented in Leinss et al. (2015), which state that at L-band (1.26 GHz), and a ρ_s of 300 kg m⁻³, the radar signal can penetrate between about 10 m at 1 % LWC and 1 m at 10 % LWC. The high quality of the phase signal ~~even with relatively high despite some snowpack~~ LWC shows promise for the overall performance of NISAR and ~~it's 6 AM and 6 AM its 0600 and 1800 LT~~ sun-synchronous orbit ~~even when snowpacks contain some LWC (Webb et al., 2021b). By processing the 12-26 February pair, we've shown that coherence can be held and quality snow phase information can be obtained at a 14 day temporal baseline, even in the presence of melt. This further supports the robustness of the technique. (Webb et al., 2021b; Bonnell et al., 2021).~~

~~Mean hourly temperature over the study period at HQ meteorologic station in VG during the study period (12-26 February). Temperatures consistently dropped below freezing at night and rose above 0°C during the most days. Blue vertical lines represent the times of the three UAVSAR acquisitions.~~

4.2 Errors and Uncertainty

Our results provide an initial evaluation of ~~the accuracy of the~~ InSAR-derived SWE ~~changes. Our comparison between the InSAR and GPR uncertainty by reporting the mean (-2.06 cm) and SD (1.56 cm) Δ SWE suggests a conservative maximum bias of ~2 cm for the area near the HQ snow pit.~~ values of snow free pixels. We note that these pixels only represent about 5 % of the study area, and much of the snow free area exists in densely forested regions where the fSCA uncertainty is greatest (Selkowitz et al., 2017). Section 4.3 outlines the continued work needed better to understand uncertainty within the InSAR SWE retrieval technique. In context with other SWE estimation techniques, airborne lidar has been shown to have

uncertainty on the order of ~~7-8-7-8~~ cm for snow depth (Currier et al., 2019) ~~that when combined with a ρ_s model with additional uncertainty of, and~~ $\sim 50 \text{ kg m}^{-3}$ ~~for modeled ρ_s (Raleigh and Small, 2017). This results in a similar to greater magnitude of SWE uncertainty for the relatively shallow snowpack that develops in the VCNP (Raleigh and Small, 2017). We anticipate the uncertainty to be reduced through future studies discussed further below. Furthermore, this method shows promise for lightly~~
590 ~~forested areas that were difficult to directly assess in our present study.~~

The atmospheric correction developed in this study is specific to the UAVSAR data we used. It assumes a homogeneous delay related to the ~~PLVLKV~~. This delay is ~~mostly-most~~ likely due to pressure and temperature differences between radar acquisitions, but does not account for smaller spatial scale water vapor variations in the atmospheric delay signal within the radar swath. While we're confident ~~in~~ the correction results ~~the method provided for the 12-19 February and 12-26 from this~~
595 ~~method for the 12-19 and 12-26~~ February pairs, the consistency of ~~near-to-far-range near-to-far range~~ phase ramp in these ~~pairs data~~ is unique within the SnowEx UAVSAR dataset, and this method won't be directly applicable to all situations.

We held the ϵ_s values constant for the entire scene. While a single value may be sufficient for the VG meadow, the entire processed scene has more topographic and climatic variation, and therefore ϵ_s and ρ_s variability within the snowpack. We used in situ ~~measured~~ ϵ_s values for this study ~~that accounted to account~~ for snowpack LWC, instead of estimating it from density like
600 ~~past studies (Rott et al., 2003; Deeb et al., 2011; ?). Eppler et al. (2022) found that error in (Rott et al., 2003; Deeb et al., 2011; Guneriusse~~
~~Eppler et al. (2022) and Leinss et al. (2015) attributed $< \sim 5\%$ Δ SWE error to ρ_s estimates only biases total SWE change by $< 5\%$ for completely dry snow. This uncertainty is likely larger in our analysis due to known~~. ~~However, due to the known presence of LWC in the snowpack and the difference in timing between ϵ_s observations and UAVSAR flights, uncertainty is likely larger in our analysis.~~ We showed that L-band InSAR ~~can-could~~ hold coherence with low ($\sim 1-5-5\%$) levels of snowpack
605 LWC. This adds complexity to the retrievals and should be the topic of future investigations. A variation in LWC between acquisitions will impact radar wave propagation speed and refraction angle in the snowpack, causing a phase shift that resembles a fluctuation in SWE, which could be either a gain or loss. The ambiguity between LWC and SWE variations affecting ϕ_{snow} is resolved by using in situ data to understand the atmospheric and snowpack dynamics between the flights. For this reason, we limited the geographic scope of this study where field teams evaluated snowpack conditions ~~in the VG meadow~~, motivated by
610 ~~of our~~ goal to confidently validate the Δ SWE retrievals.

The phase returns in this study were ~~tethered-tied~~ to a known change point using the in situ snow pit data. This method assumes that there was no variation in SWE or ϵ_s at this point between the three radar acquisitions. For future NISAR data, a time series could be initiated starting with a snow free scene. In such a scenario, any phase delay will be related to the new snow accumulated on the ground. The lack of temporal consistency of the suborbital UAVSAR measurements did not allow
615 for the implementation of this methodology ~~in this work~~.

We created new θ data using a ~~high-resolution-high-resolution~~ lidar DEM because of errors within the SRTM DEM ~~provided~~. NISAR will use the TanDEM-X derived 30 m Copernicus DEM, which does not show the same inaccuracies as SRTM ~~for non-vegetated areas~~ (Rizzoli et al., 2017), and therefore will not be of significant concern. However, all further studies utilizing SnowEx UAVSAR data should inspect the θ raster provided before employing it in the SWE change inversion equation. If errors

620 are found, new θ data should be generated using the Copernicus DEM or other methods (e.g., lidar) to minimize parameter uncertainty.

4.3 Future Work

The SnowEx 2020 and 2021 campaigns collected UAVSAR time series data at 14 different research sites across the WUS. ~~Future-While we reported a first-order estimate of uncertainty of ± 1.56 cm, future~~ analysis of this large dataset should ~~focus~~
625 ~~on-quantifying-continue to quantify~~ the uncertainties within the SWE retrieval technique. This includes but is not limited to:
(1) the impacts of θ , slope, and aspect on the SWE returns; (2) ~~the-considering the effect of snow wetness on Equation 2;~~ (3)
~~the~~ influence various forest cover metrics; (34) constructing a consistent Δ SWE time series to prepare for NISAR's 12-day
temporal repeat; and (45) implementation of spatially distributed ρ_s , ϵ_s , and LWC-data into the SWE change equation. This
could be derived from snowpack energy balance models (Marks et al., 1999; Liston and Elder, 2006) or through polarimetric
630 radar retrievals (Shi and Dozier, 2000). ~~Future NISAR InSAR SWE validation efforts would greatly benefit from synchronous
airborne lidar snow depth acquisitions with concurrent in situ measurements of ϵ_s , ρ_s , and snow depth. These efforts should
focus on complex mountain watersheds.~~

Previously, InSAR data has been used to measure geologic processes that vary at slower spatiotemporal scales than mountain
SWE, and therefore image pairs could be selectively chosen to have minimal decorrelation and atmospheric effects. However,
635 this is not the case for InSAR-based SWE monitoring, ~~-which-;~~ ~~it~~ requires a complete time series of snow accumulation and
ablation throughout the winter season ~~;~~ due to rapid decorrelation in snow covered regions.

The ability to confidently identify and correct for ~~a-~~spatially and temporally varying atmospheric signals over mountain
range scales is one of the main challenges facing this technique. To address this atmospheric limitation, additional orbital
~~snow-specific-snow-specific~~ correction methods must be developed. Future work should leverage past studies utilizing MODIS
640 and other imaging spectrometers (Li et al., 2009), ~~high-resolution-high-resolution~~ weather models (Liu et al., 2009), GPS
measurements (Li et al., 2006), and combinations of these techniques in tandem (Bekaert et al., 2015). While NISAR data
products will include ionospheric and tropospheric correction layers at 80 m spatial resolution, these corrections are automated
and may not be temporally consistent enough for snow measurement purposes.

Furthermore, while the Δ SWE results are InSAR-derived, this technique requires a ~~multi-sensor-multisensor~~ approach for
645 correct implementation. Optical fSCA data are needed to identify snow covered pixels as part of ~~the~~ correction for atmospheric
delay and to apply the SWE inversion equation over only snow covered pixels. The Landsat 8 image data used in this study
represented two of the very few ~~cloud-free-cloud-free~~ days throughout the winter time series over ~~VGNP~~~~the entire UAVSAR~~
~~swath~~. To account for the significant issue of cloud cover, future investigations should leverage ~~optical-multiple optical sensors~~
~~(e.g., Sentinel-2, MODIS, commercial high-resolution imagery, etc.), optical~~ sensor fusion and interpolation methods (Rittger
650 et al., 2021; Dozier et al., 2008), ~~and focus on how to best combine SAR and optical data for SWE change monitoring.~~
Any future SAR-derived SWE product such as the Ku- and X-band approach (Tsang et al., 2022), or the P-band Signals of
Opportunity (SoOp) (Yueh et al., 2021) will require optical data to delineate snow covered pixels in midlatitude mountain
environments, making this ~~sensor-fusion-research-multisensor approach~~ applicable for radars other than NISAR. Continued

work on how to best fuse disparate sensors through cloud computing and machine learning will be key to progressing our
655 knowledge of mountain snowpack monitoring (Durand et al., 2021).

5 Conclusions

This work leveraged ~~high-resolution~~ high-resolution (6 m) UAVSAR interferometric data products to estimate Δ SWE at
scales relevant to basin scale water resource management. We developed and applied ~~open-source processing tools to utilize a~~
workflow utilizing UAVSAR data to detect both positive and negative changes in SWE. We then used in situ snow depth ~~measurements;~~
660 ΔfSCA, and GPR ~~SWE~~ data to validate the ~~InSAR-SWE~~ InSAR-based returns. These results show the robust ability of
L-band InSAR to hold coherence and provide quality Δ SWE information even in relatively adverse conditions for radar remote
sensing. This research is the first in a series of studies analyzing the SnowEx UAVSAR dataset in preparation for the launch of
NISAR in early 2024.

NISAR's low latency (~2 days) cloud-based data products will provide the opportunity to implement this L-band InSAR
665 SWE monitoring technique at continental scales. While there is significant progress needed to better understand uncertainties
associated with the retrievals, NISAR's L-band InSAR will have the ability to ~~confidently estimate SWE variations in locations~~
~~without dense forest cover~~ estimate SWE in mountain regions globally. Spatiotemporally complete data will require ~~fusion~~
~~with optical sensors and assimilation in a multisensor approach with optical data and assimilation into~~ land surface models. We
believe that NISAR has the potential to revolutionize the way SWE is measured from spaceborne remote sensing.

670 *Code and data availability.* The code and data used to perform this analysis and create the figures are publicly available at: <https://doi.org/10.5281/zenodo.6578192>.
The uavsar_pytools package is archived at: <https://doi.org/10.5281/zenodo.6578192>. UAVSAR data are publicly available at the NASA Jet
Propulsion Laboratory UAVSAR data portal (<https://uavsar.jpl.nasa.gov/cgi-bin/data.pl>, last access: 6 March 2023) and the Alaska Satellite
Facility (ASF) Vertex data portal (<https://search.asf.alaska.edu/>). Landsat fSCA data (U.S. Geological Survey and Center, 2018) are publicly
available through the United States Geologic Survey (USGS) EarthExplorer data portal (<https://earthexplorer.usgs.gov/>, last access: 6 March
675 2023). The Western Regional Climate Center (WRCC) climate station data are publicly available (<https://wrcc.dri.edu/vallescaldera/>, last
access: 8 July 2022). SnowEx20 Jemez UNM 800 MHz MALA GPR, Version 1 data are publicly available at the NASA National Snow and
Ice Data Center Distributed Active Archive Center (NSIDC) (<https://nsidc.org/data/snowex>, last access: 4 June 2022). Information on the
SnowEx database: <https://doi.org/10.5281/zenodo.7618107>

Author contributions. JT, RWW, and HPM conceptualized the overall study. JT and RWW performed the data processing and analysis. JT,
680 RWW, and AWN drafted and edited the manuscript, with FJM and HPM providing helpful comments. AWN, HPM, and RWW provided
financial support for the study.

Competing interests. The contact author declares that none of the authors have any competing interests.

Acknowledgements. Funding for this work was provided by the NASA grant numbers NNX17AL40G (PI: Nolin), 80NSSC18K1405 (Co-I: Webb), and NNX17AL61G (PI: Marshall). Bureau of Reclamation also provided funding with grant number R21AC10459 (Webb). We
685 would like to thank Yunling Lou~~and the~~, Yang Zheng, the entire UAVSAR processing team~~;~~; Dr. Noah Molotch~~and Leanne Lestak~~, Leanne
Lestak, and Dr. Adrian Harpold for providing snow depth data~~;~~; and the SnowEx field teams, especially Adrian Marziliano, who collected
in situ observations. The authors would also like to thank Zach Keskinen, Ross Palomaki, and Naheem Adebisi for their input and review of
the code for this study.

The authors are grateful to editor Alex Langlois and reviewers Cathleen Jones and Silvan Leinss for their thorough and insightful
690 comments, which vastly improved the quality of this manuscript.

References

- A2 Photonic WISe, <https://a2photonicsensors.com/wise-sensor-liquid-water-content-snow/>, 2021.
- Bales, R. C., Molotch, N. P., Painter, T. H., Dettinger, M. D., Rice, R., and Dozier, J.: Mountain Hydrology of the Western United States, *Water Resources Research*, 42, <https://doi.org/10.1029/2005WR004387>, 2006.
- 695 Balzter, H.: Forest Mapping and Monitoring with Interferometric Synthetic Aperture Radar (InSAR), *Progress in Physical Geography: Earth and Environment*, 25, 159–177, <https://doi.org/10.1177/030913330102500201>, 2001.
- Bekaert, D., Walters, R., Wright, T., Hooper, A., and Parker, D.: Statistical Comparison of InSAR Tropospheric Correction Techniques, *Remote Sensing of Environment*, 170, 40–47, <https://doi.org/10.1016/j.rse.2015.08.035>, 2015.
- Bekaert, D. P., Jones, C. E., An, K., and Huang, M.-H.: Exploiting UAVSAR for a Comprehensive Analysis of Subsidence in the Sacramento
700 Delta, *Remote Sensing of Environment*, 220, 124–134, <https://doi.org/10.1016/j.rse.2018.10.023>, 2018.
- Bonnell, R., McGrath, D., Williams, K., Webb, R., Fassnacht, S. R., and Marshall, H.-P.: Spatiotemporal Variations in Liquid Water Content in a Seasonal Snowpack: Implications for Radar Remote Sensing, *Remote Sensing*, 13, 4223, <https://doi.org/10.3390/rs13214223>, 2021.
- Bradford, J. H., Clement, W. P., and Barrash, W.: Estimating Porosity with Ground-Penetrating Radar Reflection Tomography: A Controlled
705 3-D Experiment at the Boise Hydrogeophysical Research Site, *Water Resources Research*, 45, <https://doi.org/10.1029/2008WR006960>, 2009.
- Chen, C. W. and Zebker, H. A.: Two-Dimensional Phase Unwrapping with Use of Statistical Models for Cost Functions in Nonlinear Optimization, *Journal of the Optical Society of America A*, 18, 338, <https://doi.org/10.1364/JOSAA.18.000338>, 2001.
- Colesanti, C., Ferretti, A., Prati, C., and Rocca, F.: Monitoring Landslides and Tectonic Motions with the Permanent Scatterers Technique, *Engineering Geology*, 68, 3–14, [https://doi.org/10.1016/S0013-7952\(02\)00195-3](https://doi.org/10.1016/S0013-7952(02)00195-3), 2003.
- 710 Conde, V., Nico, G., Mateus, P., Catalão, J., Kontu, A., and Gritsevich, M.: On The Estimation of Temporal Changes of Snow Water Equivalent by Spaceborne Sar Interferometry: A New Application for the Sentinel-1 Mission, *Journal of Hydrology and Hydromechanics*, 67, 93–100, <https://doi.org/10.2478/johh-2018-0003>, 2019.
- Conger, S. M. and McClung, D. M.: Comparison of Density Cutters for Snow Profile Observations, *Journal of Glaciology*, 55, 163–169, <https://doi.org/10.3189/002214309788609038>, 2009.
- 715 Currier, W. R., Pflug, J., Mazzotti, G., Jonas, T., Deems, J. S., Bormann, K. J., Painter, T. H., Hiemstra, C. A., Gelvin, A., Uhlmann, Z., Spaete, L., Glenn, N. F., and Lundquist, J. D.: Comparing Aerial Lidar Observations With Terrestrial Lidar and Snow-Probe Transects From NASA’s 2017 SnowEx Campaign, *Water Resources Research*, 55, 6285–6294, <https://doi.org/10.1029/2018WR024533>, 2019.
- Danklmayer, A., Doring, B., Schwerdt, M., and Chandra, M.: Assessment of Atmospheric Propagation Effects in SAR Images, *IEEE Transactions on Geoscience and Remote Sensing*, 47, 3507–3518, <https://doi.org/10.1109/TGRS.2009.2022271>, 2009.
- 720 Deeb, E. J., Forster, R. R., and Kane, D. L.: Monitoring Snowpack Evolution Using Interferometric Synthetic Aperture Radar on the North Slope of Alaska, USA, *International Journal of Remote Sensing*, 32, 3985–4003, <https://doi.org/10.1080/01431161003801351>, 2011.
- Deems, J. S., Fassnacht, S. R., and Elder, K. J.: Fractal Distribution of Snow Depth from Lidar Data, *Journal of Hydrometeorology*, 7, 285–297, <https://doi.org/10.1175/JHM487.1>, 2006.
- Derksen, C., Walker, A., LeDrew, E., and Goodison, B.: Time-Series Analysis of Passive-Microwave-Derived Central North American Snow
725 Water Equivalent Imagery, *Annals of Glaciology*, 34, 1–7, <https://doi.org/10.3189/172756402781817815>, 2002.
- Dozier, J., Painter, T. H., Rittger, K., and Frew, J. E.: Time–Space Continuity of Daily Maps of Fractional Snow Cover and Albedo from MODIS, *Advances in Water Resources*, 31, 1515–1526, <https://doi.org/10.1016/j.advwatres.2008.08.011>, 2008.

- Durand, M., Barros, A., Dozier, J., Adler, R., Cooley, S., Entekhabi, D., Forman, B. A., Konings, A. G., Kustas, W. P., Lundquist, J. D., Pavelsky, T. M., Rodell, M., and Steele-Dunne, S.: Achieving Breakthroughs in Global Hydrologic Science by Unlocking the Power of Multisensor, Multidisciplinary Earth Observations, *AGU Advances*, 2, e2021AV000455, <https://doi.org/10.1029/2021AV000455>, 2021.
- Eiriksson, D., Whitson, M., Luce, C. H., Marshall, H. P., Bradford, J., Benner, S. G., Black, T., Hetrick, H., and McNamara, J. P.: An Evaluation of the Hydrologic Relevance of Lateral Flow in Snow at Hillslope and Catchment Scales: LATERAL FLOW IN SNOW, *Hydrological Processes*, 27, 640–654, <https://doi.org/10.1002/hyp.9666>, 2013.
- Eppler, J., Rabus, B., and Morse, P.: Snow Water Equivalent Change Mapping from Slope-Correlated Synthetic Aperture Radar Interferometry (InSAR) Phase Variations, *The Cryosphere*, 16, 1497–1521, <https://doi.org/10.5194/tc-16-1497-2022>, 2022.
- Evans, S. L., Flores, A. N., Heilig, A., Kohn, M. J., Marshall, H.-P., and McNamara, J. P.: Isotopic Evidence for Lateral Flow and Diffusive Transport, but Not Sublimation, in a Sloped Seasonal Snowpack, Idaho, USA, *Geophysical Research Letters*, 43, 3298–3306, <https://doi.org/10.1002/2015GL067605>, 2016.
- Farr, T. G., Rosen, P. A., Caro, E., Crippen, R., Duren, R., Hensley, S., Kobrick, M., Paller, M., Rodriguez, E., Roth, L., Seal, D., Shaffer, S., Shimada, J., Umland, J., Werner, M., Oskin, M., Burbank, D., and Alsdorf, D.: The Shuttle Radar Topography Mission, *Reviews of Geophysics*, 45, <https://doi.org/10.1029/2005RG000183>, 2007.
- Ferretti, A., Prati, C., and Rocca, F.: Permanent Scatterers in SAR Interferometry, *IEEE Transactions on Geoscience and Remote Sensing*, 39, 8–20, <https://doi.org/10.1109/36.898661>, 2001.
- Foster, J. L., Sun, C., Walker, J. P., Kelly, R., Chang, A., Dong, J., and Powell, H.: Quantifying the Uncertainty in Passive Microwave Snow Water Equivalent Observations, *Remote Sensing of Environment*, 94, 187–203, <https://doi.org/10.1016/j.rse.2004.09.012>, 2005.
- Funning, G. J., Parsons, B., Wright, T. J., Jackson, J. A., and Fielding, E. J.: Surface Displacements and Source Parameters of the 2003 Bam (Iran) Earthquake from Envisat Advanced Synthetic Aperture Radar Imagery, *Journal of Geophysical Research: Solid Earth*, 110, <https://doi.org/10.1029/2004JB003338>, 2005.
- Goldstein, R. M. and Zebker, H. A.: Interferometric Radar Measurement of Ocean Surface Currents, *Nature*, 328, 707–709, <https://doi.org/10.1038/328707a0>, 1987.
- Goldstein, R. M., Zebker, H. A., and Werner, C. L.: Satellite Radar Interferometry: Two-dimensional Phase Unwrapping, *Radio Science*, 23, 713–720, <https://doi.org/10.1029/RS023i004p00713>, 1988.
- Gubler, H. and Hiller, M.: The Use of Microwave FMCW Radar in Snow and Avalanche Research, *Cold Regions Science and Technology*, 9, 109–119, [https://doi.org/10.1016/0165-232X\(84\)90003-X](https://doi.org/10.1016/0165-232X(84)90003-X), 1984.
- Guneriussen, T., Hogda, K., Johnsen, H., and Lauknes, I.: InSAR for Estimation of Changes in Snow Water Equivalent of Dry Snow, *IEEE Transactions on Geoscience and Remote Sensing*, 39, 2101–2108, <https://doi.org/10.1109/36.957273>, 2001.
- Harpold, A., Molotch, N. P., Musselman, K. N., Bales, R. C., Kirchner, P. B., Litvak, M., and Brooks, P. D.: Soil Moisture Response to Snowmelt Timing in Mixed-Conifer Subalpine Forests, *Hydrological Processes*, 29, 2782–2798, <https://doi.org/10.1002/hyp.10400>, 2015.
- Heilig, A., Mitterer, C., Schmid, L., Wever, N., Schweizer, J., Marshall, H.-P., and Eisen, O.: Seasonal and Diurnal Cycles of Liquid Water in Snow—Measurements and Modeling, *Journal of Geophysical Research: Earth Surface*, 120, 2139–2154, <https://doi.org/10.1002/2015JF003593>, 2015.
- Hensley, S., Wheeler, K., Sadowy, G., Jones, C., Shaffer, S., Zebker, H., Miller, T., Heavey, B., Chuang, E., Chao, R., Vines, K., Nishimoto, K., Prater, J., Carrico, B., Chamberlain, N., Shimada, J., Simard, M., Chapman, B., Muellerschoen, R., Le, C., Michel, T., Hamilton, G., Robison, D., Neumann, G., Meyer, R., Smith, P., Granger, J., Rosen, P., Flower, D., and Smith, R.: The UAVSAR Instrument: Description and First Results, in: 2008 IEEE Radar Conference, pp. 1–6, IEEE, Rome, Italy, <https://doi.org/10.1109/RADAR.2008.4720722>, 2008.

- Holbrook, W. S., Miller, S. N., and Provar, M. A.: Estimating Snow Water Equivalent over Long Mountain Transects Using Snowmobile-Mounted Ground-Penetrating Radar, *GEOPHYSICS*, 81, WA183–WA193, <https://doi.org/10.1190/geo2015-0121.1>, 2016.
- Johnson, M. and Sandusky, M.: SnowEx/Snowex_db: SnowEx Hackweek 2022 Release, Zenodo, <https://doi.org/10.5281/zenodo.7618108>, 2023.
- 770 Keskinen, Z. and Tarricone, J.: Uavsar_pytools, Zenodo, <https://doi.org/10.5281/zenodo.6789624>, 2022.
- King, J., Derksen, C., Toose, P., Langlois, A., Larsen, C., Lemmetyinen, J., Marsh, P., Montpetit, B., Roy, A., Rutter, N., and Sturm, M.: The Influence of Snow Microstructure on Dual-Frequency Radar Measurements in a Tundra Environment, *Remote Sensing of Environment*, 215, 242–254, <https://doi.org/10.1016/j.rse.2018.05.028>, 2018.
- Leinss, S., Wiesmann, A., Lemmetyinen, J., and Hajnsek, I.: Snow Water Equivalent of Dry Snow Measured by Differential Interferometry, *IEEE Journal of Selected Topics in Applied Earth Observations and Remote Sensing*, 8, 3773–3790, <https://doi.org/10.1109/JSTARS.2015.2432031>, 2015.
- 775 Lettenmaier, D. P., Alsdorf, D., Dozier, J., Huffman, G. J., Pan, M., and Wood, E. F.: Inroads of Remote Sensing into Hydrologic Science during the WRR Era, *Water Resources Research*, 51, 7309–7342, <https://doi.org/10.1002/2015WR017616>, 2015.
- Lewis, G., Osterberg, E., Hawley, R., Whitmore, B., Marshall, H. P., and Box, J.: Regional Greenland Accumulation Variability from Operation IceBridge Airborne Accumulation Radar, *The Cryosphere*, 11, 773–788, <https://doi.org/10.5194/tc-11-773-2017>, 2017.
- 780 Li, D., Wrzesien, M. L., Durand, M., Adam, J., and Lettenmaier, D. P.: How Much Runoff Originates as Snow in the Western United States, and How Will That Change in the Future?: Western U.S. Snowmelt-Derived Runoff, *Geophysical Research Letters*, 44, 6163–6172, <https://doi.org/10.1002/2017GL073551>, 2017a.
- Li, H., Wang, Z., He, G., and Man, W.: Estimating Snow Depth and Snow Water Equivalence Using Repeat-Pass Interferometric SAR in the Northern Piedmont Region of the Tianshan Mountains, *Journal of Sensors*, 2017, 1–17, <https://doi.org/10.1155/2017/8739598>, 2017b.
- 785 Li, Z., Fielding, E. J., Cross, P., and Muller, J.-P.: Interferometric Synthetic Aperture Radar Atmospheric Correction: GPS Topography-Dependent Turbulence Model: INTEGRATION OF GPS AND INSAR, *Journal of Geophysical Research: Solid Earth*, 111, n/a–n/a, <https://doi.org/10.1029/2005JB003711>, 2006.
- Li, Z., Fielding, E. J., Cross, P., and Preusker, R.: Advanced InSAR Atmospheric Correction: MERIS/MODIS Combination and Stacked Water Vapour Models, *International Journal of Remote Sensing*, 30, 3343–3363, <https://doi.org/10.1080/01431160802562172>, 2009.
- 790 Lievens, H., Demuzere, M., Marshall, H.-P., Reichle, R. H., Brucker, L., Brangers, I., de Rosnay, P., Dumont, M., Girotto, M., Immerzeel, W. W., Jonas, T., Kim, E. J., Koch, I., Marty, C., Saloranta, T., Schöber, J., and De Lannoy, G. J. M.: Snow Depth Variability in the Northern Hemisphere Mountains Observed from Space, *Nature Communications*, 10, 4629, <https://doi.org/10.1038/s41467-019-12566-y>, 2019.
- 795 Lievens, H., Brangers, I., Marshall, H.-P., Jonas, T., Olefs, M., and De Lannoy, G.: Sentinel-1 Snow Depth Retrieval at Sub-Kilometer Resolution over the European Alps, *The Cryosphere*, 16, 159–177, <https://doi.org/10.5194/tc-16-159-2022>, 2022.
- Liston, G. E. and Elder, K.: A Distributed Snow-Evolution Modeling System (SnowModel), *Journal of Hydrometeorology*, 7, 1259–1276, <https://doi.org/10.1175/JHM548.1>, 2006.
- 800 Liu, S., Hanssen, R., and Mika, Á.: On the Value of High-Resolution Weather Models for Atmospheric Mitigation in SAR Interferometry, in: 2009 IEEE International Geoscience and Remote Sensing Symposium, vol. 2, pp. II-749–II-752, <https://doi.org/10.1109/IGARSS.2009.5418199>, 2009.
- Lund, J., Forster, R. R., Rupper, S. B., Deeb, E. J., Marshall, H. P., Hashmi, M. Z., and Burgess, E.: Mapping Snowmelt Progression in the Upper Indus Basin With Synthetic Aperture Radar, *Frontiers in Earth Science*, 7, 318, <https://doi.org/10.3389/feart.2019.00318>, 2020.

- Marks, D., Domingo, J., Susong, D., Link, T., and Garen, D.: A Spatially Distributed Energy Balance Snowmelt Model for Application
805 in Mountain Basins, *Hydrological Processes*, 13, 1935–1959, [https://doi.org/10.1002/\(SICI\)1099-1085\(199909\)13:12/13<1935::AID-HYP868>3.0.CO;2-C](https://doi.org/10.1002/(SICI)1099-1085(199909)13:12/13<1935::AID-HYP868>3.0.CO;2-C), 1999.
- Marshall, H., Vuyovich, C., Hiemstra, C., Brucker, L., Elder, K., Deems, J., and Newlin, J.: NASA SnowEx 2020 Experiment Plan, Tech. rep., https://snow.nasa.gov/sites/default/files/NASA_SnowEx_Experiment_Plan_v15_draft.pdf, 2019.
- Marshall, H., Deeb, E., Forster, R., Vuyovich, C., Elder, K., Hiemstra, C., and Lund, J.: L-Band InSAR Depth Retrieval During the NASA
810 SnowEx 2020 Campaign: Grand Mesa, Colorado, in: 2021 IEEE International Geoscience and Remote Sensing Symposium IGARSS, pp. 625–627, <https://doi.org/10.1109/IGARSS47720.2021.9553852>, 2021.
- Marshall, H.-P. and Koh, G.: FMCW Radars for Snow Research, *Cold Regions Science and Technology*, 52, 118–131, <https://doi.org/10.1016/j.coldregions.2007.04.008>, 2008.
- Marshall, H.-P., Koh, G., and Forster, R. R.: Estimating Alpine Snowpack Properties Using FMCW Radar, *Annals of Glaciology*, 40, 157–
815 162, <https://doi.org/10.3189/172756405781813500>, 2005.
- Marshall, H.-P., Mason, M., McCormick, M., Craaybeek, D., Elder, K., Vuyovich, C., and Time Series Site Leads and Field Teams: SnowEx20
Time Series Snow Pit Measurements [Jemez River]. [Date Accessed: 14 October 2022]., <https://doi.org/10.5067/POT9E0FFUUD1>, 2022.
- McGrath, D., Sass, L., O’Neel, S., McNeil, C., Candela, S. G., Baker, E. H., and Marshall, H.-P.: Interannual Snow Accumulation Vari-
ability on Glaciers Derived from Repeat, Spatially Extensive Ground-Penetrating Radar Surveys, *The Cryosphere*, 12, 3617–3633,
820 <https://doi.org/10.5194/tc-12-3617-2018>, 2018.
- McGrath, D., Webb, R., Shean, D., Bonnell, R., Marshall, H.-P., Painter, T. H., Molotch, N. P., Elder, K., Hiemstra, C., and Brucker, L.:
Spatially Extensive Ground-Penetrating Radar Snow Depth Observations During NASA’s 2017 SnowEx Campaign: Comparison With In
Situ, Airborne, and Satellite Observations, *Water Resources Research*, 55, 10026–10036, <https://doi.org/10.1029/2019WR024907>, 2019.
- Meyer, F. J.: Performance Requirements for Ionospheric Correction of Low-Frequency SAR Data, *IEEE Transactions on Geoscience and*
825 *Remote Sensing*, 49, 3694–3702, <https://doi.org/10.1109/TGRS.2011.2146786>, 2011.
- Michaelides, R. J., Chen, R. H., Zhao, Y., Schaefer, K., Parsekian, A. D., Sullivan, T., Moghaddam, M., Zebker, H. A., Liu, L., Xu, X.,
and Chen, J.: Permafrost Dynamics Observatory—Part I: Postprocessing and Calibration Methods of UAVSAR L-Band InSAR Data for
Seasonal Subsidence Estimation, *Earth and Space Science*, 8, <https://doi.org/10.1029/2020EA001630>, 2021.
- Milly, P. C. D., Betancourt, J., Falkenmark, M., Hirsch, R. M., Kundzewicz, Z. W., Lettenmaier, D. P., and Stouffer, R. J.: Stationarity Is
830 Dead: Whither Water Management?, *Science*, 319, 573–574, <https://doi.org/10.1126/science.1151915>, 2008.
- Molotch, N. P., Brooks, P. D., Burns, S. P., Litvak, M., Monson, R. K., McConnell, J. R., and Musselman, K.: Ecohydrological Controls on
Snowmelt Partitioning in Mixed-Conifer Sub-Alpine Forests, *Ecohydrology*, 2, 129–142, <https://doi.org/10.1002/eco.48>, 2009.
- Mote, P. W., Li, S., Lettenmaier, D. P., Xiao, M., and Engel, R.: Dramatic Declines in Snowpack in the Western US, *npj Climate and*
Atmospheric Science, 1, 2, <https://doi.org/10.1038/s41612-018-0012-1>, 2018.
- 835 Mouginit, J.: Mapping of Ice Motion in Antarctica Using Synthetic-Aperture Radar Data, p. 15, 2012.
- Musselman, K. N., Molotch, N. P., and Brooks, P. D.: Effects of Vegetation on Snow Accumulation and Ablation in a Mid-Latitude Sub-
Alpine Forest, *Hydrological Processes*, 22, 2767–2776, <https://doi.org/10.1002/hyp.7050>, 2008.
- Nagler, T. and Rott, H.: Retrieval of Wet Snow by Means of Multitemporal SAR Data, *IEEE Transactions on Geoscience and Remote*
Sensing, 38, 754–765, <https://doi.org/10.1109/36.842004>, 2000.
- 840 Nagler, T., Rott, H., Ripper, E., Bippus, G., and Hetzenecker, M.: Advancements for Snowmelt Monitoring by Means of Sentinel-1 SAR,
Remote Sensing, 8, 348, <https://doi.org/10.3390/rs8040348>, 2016.

- Nagler, T., Rott, H., Scheiblauer, S., Libert, L., Mölg, N., Horn, R., Fischer, J., Keller, M., Moreira, A., and Kubanek, J.: Airborne Experiment on Insar Snow Mass Retrieval in Alpine Environment, in: IGARSS 2022 - 2022 IEEE International Geoscience and Remote Sensing Symposium, pp. 4549–4552, <https://doi.org/10.1109/IGARSS46834.2022.9883809>, 2022.
- 845 Nolin, A., Dozier, J., and Mertes, L.: Mapping Alpine Snow Using a Spectral Mixture Modeling Technique, *Annals of Glaciology*, 17, 121–124, <https://doi.org/doi:10.3189/S0260305500012702>, 1993.
- OpenTopography: Jemez River Basin Snow-off LiDAR Survey, <https://opentopography.org/meta/OT.062012.26913.1>, 2012.
- Painter, T. H., Rittger, K., McKenzie, C., Slaughter, P., Davis, R. E., and Dozier, J.: Retrieval of Subpixel Snow Covered Area, Grain Size, and Albedo from MODIS, *Remote Sensing of Environment*, 113, 868–879, <https://doi.org/10.1016/j.rse.2009.01.001>, 2009.
- 850 Painter, T. H., Berisford, D. F., Boardman, J. W., Bormann, K. J., Deems, J. S., Gehrke, F., Hedrick, A., Joyce, M., Laidlaw, R., Marks, D., Mattmann, C., McGurk, B., Ramirez, P., Richardson, M., Skiles, S. M., Seidel, F. C., and Winstral, A.: The Airborne Snow Observatory: Fusion of Scanning Lidar, Imaging Spectrometer, and Physically-Based Modeling for Mapping Snow Water Equivalent and Snow Albedo, *Remote Sensing of Environment*, 184, 139–152, <https://doi.org/10.1016/j.rse.2016.06.018>, 2016.
- Poland, M. P. and Zebker, H. A.: Volcano Geodesy Using InSAR in 2020: The Past and next Decades, *Bulletin of Volcanology*, 84, 27, 855 <https://doi.org/10.1007/s00445-022-01531-1>, 2022.
- Proksch, M., Rutter, N., Fierz, C., and Schneebeli, M.: Intercomparison of Snow Density Measurements: Bias, Precision, and Vertical Resolution, *The Cryosphere*, 10, 371–384, <https://doi.org/10.5194/tc-10-371-2016>, 2016.
- Raleigh, M. S. and Small, E. E.: Snowpack Density Modeling Is the Primary Source of Uncertainty When Mapping Basin-Wide SWE with Lidar: Uncertainties in SWE Mapping With Lidar, *Geophysical Research Letters*, 44, 3700–3709, <https://doi.org/10.1002/2016GL071999>, 860 2017.
- Rango, A., Chang, A. T. C., and Foster, J. L.: The Utilization of Spaceborne Microwave Radiometers for Monitoring Snowpack Properties, *Hydrology Research*, 10, 25–40, <https://doi.org/10.2166/nh.1979.0003>, 1979.
- Rittger, K., Krock, M., Kleiber, W., Bair, E. H., Brodzik, M. J., Stephenson, T. R., Rajagopalan, B., Bormann, K. J., and Painter, T. H.: Multi-Sensor Fusion Using Random Forests for Daily Fractional Snow Cover at 30 m, *Remote Sensing of Environment*, 264, 112608, 865 <https://doi.org/10.1016/j.rse.2021.112608>, 2021.
- Rizzoli, P., Martone, M., Gonzalez, C., Wecklich, C., Borla Tridon, D., Bräutigam, B., Bachmann, M., Schulze, D., Fritz, T., Huber, M., Wessel, B., Krieger, G., Zink, M., and Moreira, A.: Generation and Performance Assessment of the Global TanDEM-X Digital Elevation Model, *ISPRS Journal of Photogrammetry and Remote Sensing*, 132, 119–139, <https://doi.org/10.1016/j.isprsjprs.2017.08.008>, 2017.
- Rodríguez, E., Morris, C. S., and Belz, J. E.: A Global Assessment of the SRTM Performance, *Photogrammetric Engineering & Remote* 870 *Sensing*, 72, 249–260, <https://doi.org/10.14358/PERS.72.3.249>, 2006.
- Rosen, P., Hensley, S., Joughin, I., Li, F., Madsen, S., Rodriguez, E., and Goldstein, R.: Synthetic Aperture Radar Interferometry, *Proceedings of the IEEE*, 88, 333–382, <https://doi.org/10.1109/5.838084>, 2000.
- Rosen, P., Hensley, S., Wheeler, K., Sadowy, G., Miller, T., Shaffer, S., Muellerschoen, R., Jones, C., Zebker, H., and Madsen, S.: UAVSAR: A New NASA Airborne SAR System for Science and Technology Research, in: 2006 IEEE Conference on Radar, pp. 22–29, IEEE, 875 Syracuse, NY, USA, <https://doi.org/10.1109/RADAR.2006.1631770>, 2006.
- Rosen, P., Hensley, S., Shaffer, S., Edelstein, W., Kim, Y., Kumar, R., Misra, T., Bhan, R., and Sagi, R.: The NASA-ISRO SAR (NISAR) Mission Dual-Band Radar Instrument Preliminary Design, in: 2017 IEEE International Geoscience and Remote Sensing Symposium (IGARSS), pp. 3832–3835, <https://doi.org/10.1109/IGARSS.2017.8127836>, 2017.

- Rott, H., Nagler, T., and Scheiber, R.: Snow Mass Retrieval by Means of SAR Interferometry, in: FRINGE '03 Workshop: Advances in SAR Interferometry from ERS and ENVISAT Missions, pp. pp. 1–6, Noordwijk: European Space Agency (ESA) Publications Division, Frascati, Italy, 2003.
- Rott, H., Yueh, S. H., Cline, D. W., Duguay, C., Essery, R., Haas, C., Hélière, F., Kern, M., Macelloni, G., Malnes, E., Nagler, T., Pulliainen, J., Rebhan, H., and Thompson, A.: Cold Regions Hydrology High-Resolution Observatory for Snow and Cold Land Processes, *Proceedings of the IEEE*, 98, 752–765, <https://doi.org/10.1109/JPROC.2009.2038947>, 2010.
- Rutter, N., Sandells, M. J., Derksen, C., King, J., Toose, P., Wake, L., Watts, T., Essery, R., Roy, A., Royer, A., Marsh, P., Larsen, C., and Sturm, M.: Effect of Snow Microstructure Variability on Ku-band Radar Snow Water Equivalent Retrievals, *The Cryosphere*, 13, 3045–3059, <https://doi.org/10.5194/tc-13-3045-2019>, 2019.
- Ryan, W. A., Doesken, N. J., and Fassnacht, S. R.: Evaluation of Ultrasonic Snow Depth Sensors for U.S. Snow Measurements, *Journal of Atmospheric and Oceanic Technology*, 25, 667–684, <https://doi.org/10.1175/2007JTECHA947.1>, 2008.
- Sandmeier, K.-J.: REFLEXW, <https://www.sandmeier-geo.de/reflexw.html>, 2022.
- Selkowitz, D. J., Painter, T. H., Rittger, K., Schmidt, G., and Forster, R.: The USGS Landsat Snow Covered Area Products: Methods and Preliminary Validation, Tech. rep., 2017.
- Shi, J. and Dozier, J.: Estimation of Snow Water Equivalence Using SIR-C/X-SAR. II. Inferring Snow Depth and Particle Size, *IEEE Transactions on Geoscience and Remote Sensing*, 38, 2475–2488, <https://doi.org/10.1109/36.885196>, 2000.
- Siirila-Woodburn, E. R., Rhoades, A. M., Hatchett, B. J., Huning, L. S., Szinai, J., Tague, C., Nico, P. S., Feldman, D. R., Jones, A. D., Collins, W. D., and Kaatz, L.: A Low-to-No Snow Future and Its Impacts on Water Resources in the Western United States, *Nature Reviews Earth & Environment*, <https://doi.org/10.1038/s43017-021-00219-y>, 2021.
- Stewart, I. T., Cayan, D. R., and Dettinger, M. D.: Changes in Snowmelt Runoff Timing in Western North America under a ‘Business as Usual’ Climate Change Scenario, *Climatic Change*, 62, 217–232, <https://doi.org/10.1023/B:CLIM.0000013702.22656.e8>, 2004.
- Stillinger, T., Rittger, K., Raleigh, M. S., Michell, A., Davis, R. E., and Bair, E. H.: Landsat, MODIS, and VIIRS Snow Cover Mapping Algorithm Performance as Validated by Airborne Lidar Datasets, *The Cryosphere*, 17, 567–590, <https://doi.org/10.5194/tc-17-567-2023>, 2023.
- Sun, G., Ranson, K., Kharuk, V., and Kovacs, K.: Validation of Surface Height from Shuttle Radar Topography Mission Using Shuttle Laser Altimeter, *Remote Sensing of Environment*, 88, 401–411, <https://doi.org/10.1016/j.rse.2003.09.001>, 2003.
- Tarricone, J.: Estimating Snow Accumulation and Ablation with L-band InSAR: Code and Data for Analysis and Figure Creation, Zenodo, <https://doi.org/10.5281/zenodo.7730470>, 2023.
- Trujillo, E., Ramírez, J. A., and Elder, K. J.: Topographic, Meteorologic, and Canopy Controls on the Scaling Characteristics of the Spatial Distribution of Snow Depth Fields, *Water Resources Research*, 43, <https://doi.org/10.1029/2006WR005317>, 2007.
- Tsai, Y.-L. S., Dietz, A., Oppelt, N., and Kuenzer, C.: Remote Sensing of Snow Cover Using Spaceborne SAR: A Review, *Remote Sensing*, 11, 1456, <https://doi.org/10.3390/rs11121456>, 2019.
- Tsang, L., Durand, M., Derksen, C., Barros, A. P., Kang, D.-H., Lievens, H., Marshall, H.-P., Zhu, J., Johnson, J., King, J., Lemmetyinen, J., Sandells, M., Rutter, N., Siqueira, P., Nolin, A., Osmanoglu, B., Vuyovich, C., Kim, E., Taylor, D., Merkouriadi, I., Brucker, L., Navari, M., Dumont, M., Kelly, R., Kim, R. S., Liao, T.-H., Borah, F., and Xu, X.: Review Article: Global Monitoring of Snow Water Equivalent Using High-Frequency Radar Remote Sensing, *The Cryosphere*, 16, 3531–3573, <https://doi.org/10.5194/tc-16-3531-2022>, 2022.
- Ulaby, F. T., Stiles, W. H., and Abdelrazik, M.: Snowcover Influence on Backscattering from Terrain, *IEEE Transactions on Geoscience and Remote Sensing*, GE-22, 126–133, <https://doi.org/10.1109/TGRS.1984.350604>, 1984.

- U.S. Geological Survey, E. R. O. and Center, S.: Collection-1 Landsat Level-3 Fractional Snow Covered Area (FSCA) Science Product, <https://doi.org/10.5066/F7XK8DS5>, 2018.
- 920 Vuyovich, C. M., Jacobs, J. M., and Daly, S. F.: Comparison of Passive Microwave and Modeled Estimates of Total Watershed SWE in the Continental United States, *Water Resources Research*, 50, 9088–9102, <https://doi.org/10.1002/2013WR014734>, 2014.
- Webb, R.: SnowEx20 Jemez UNM 800 MHz MALA GPR, Version 1, <https://doi.org/10.5067/H38Q5FTBPZ8K>, 2020.
- Webb, R. W.: Using Ground Penetrating Radar to Assess the Variability of Snow Water Equivalent and Melt in a Mixed Canopy Forest, Northern Colorado, *Frontiers of Earth Science*, 11, 482–495, <https://doi.org/10.1007/s11707-017-0645-0>, 2017.
- 925 Webb, R. W., Jennings, K. S., Fend, M., and Molotch, N. P.: Combining Ground-Penetrating Radar With Terrestrial LiDAR Scanning to Estimate the Spatial Distribution of Liquid Water Content in Seasonal Snowpacks, *Water Resources Research*, 54, <https://doi.org/10.1029/2018WR022680>, 2018.
- Webb, R. W., Jennings, K., Finsterle, S., and Fassnacht, S. R.: Two-Dimensional Liquid Water Flow through Snow at the Plot Scale in Continental Snowpacks: Simulations and Field Data Comparisons, *The Cryosphere*, 15, 1423–1434, <https://doi.org/10.5194/tc-15-1423-2021>, 2021a.
- 930 Webb, R. W., Marziliano, A., McGrath, D., Bonnell, R., Meehan, T. G., Vuyovich, C., and Marshall, H.-P.: In Situ Determination of Dry and Wet Snow Permittivity: Improving Equations for Low Frequency Radar Applications, *Remote Sensing*, 13, 4617, <https://doi.org/10.3390/rs13224617>, 2021b.
- Yu, C., Li, Z., and Penna, N. T.: Interferometric Synthetic Aperture Radar Atmospheric Correction Using a GPS-based Iterative Tropospheric Decomposition Model, *Remote Sensing of Environment*, 204, 109–121, <https://doi.org/10.1016/j.rse.2017.10.038>, 2018.
- 935 Yueh, S. H., Dinardo, S. J., Akgiray, A., West, R., Cline, D. W., and Elder, K.: Airborne Ku-Band Polarimetric Radar Remote Sensing of Terrestrial Snow Cover, *IEEE Transactions on Geoscience and Remote Sensing*, 47, 3347–3364, <https://doi.org/10.1109/TGRS.2009.2022945>, 2009.
- Yueh, S. H., Shah, R., Xu, X., Stiles, B., and Bosch-Lluis, X.: A Satellite Synthetic Aperture Radar Concept Using P-Band Signals of Opportunity, *IEEE Journal of Selected Topics in Applied Earth Observations and Remote Sensing*, 14, 2796–2816, <https://doi.org/10.1109/JSTARS.2021.3059242>, 2021.
- 940 Zebker, H. A. and Goldstein, R. M.: Topographic Mapping from Interferometric Synthetic Aperture Radar Observations, *Journal of Geophysical Research: Solid Earth*, 91, 4993–4999, <https://doi.org/10.1029/JB091iB05p04993>, 1986.
- Zebker, H. A., Rosen, P. A., and Hensley, S.: Atmospheric Effects in Interferometric Synthetic Aperture Radar Surface Deformation and Topographic Maps, *Journal of Geophysical Research: Solid Earth*, 102, 7547–7563, <https://doi.org/10.1029/96JB03804>, 1997.
- 945 Zhu, J., Tan, S., Tsang, L., Kang, D.-H., and Kim, E.: Snow Water Equivalent Retrieval Using Active and Passive Microwave Observations, *Water Resources Research*, 57, e2020WR027563, <https://doi.org/10.1029/2020WR027563>, 2021.